# UC Berkeley
## UC Berkeley Previously Published Works

**Title**
Multidisciplinary Constraints on the Abundance of Diamond and Eclogite in the Cratonic Lithosphere

**Authors**
Garber, JM
Maurya, S
Hernandez, JA
et al.
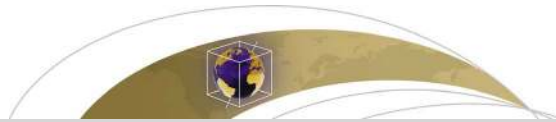
**RESEARCH ARTICLE**

**Key Points:**
- We used forward modeling to explain high shear-wave velocities in the cratonic lithosphere observed in seismic tomography models
- Our best estimate for the cause of high shear-wave velocities in the cratonic lithosphere is ≤20 vol.% eclogite and ~2 vol.% diamond
- Our diamond estimate comports with global carbon mass balance constraints and could have been implanted over reasonable timescales

**Supporting Information:**
- Supporting Information S1
- Data Set S1
- Data Set S2
- Data Set S3
- Data Set S4
- Data Set S5
- Data Set S6
- Data Set S7
- Data Set S8
- Data Set S9
- Data Set S10

**Correspondence to:**
J. M. Garber,
jxg1395@psu.edu

# Multidisciplinary Constraints on the Abundance of Diamond and Eclogite in the Cratonic Lithosphere

Joshua M. Garber[1,2], Satish Maurya[3,4], Jean-Alexis Hernandez[5], Megan S. Duncan[6,7], Li Zeng[8], Hongluo L. Zhang[9], Ulrich Faul[10], Catherine McCammon[11], Jean-Paul Montagner[3], Louis Moresi[12], Barbara A. Romanowicz[4,13], Roberta L. Rudnick[1], and Lars Stixrude[14]

[1]Department of Earth Science, University of California, Santa Barbara, CA, USA, [2]Now at Department of Geosciences, Pennsylvania State University, University Park, PA, USA, [3]Institut de Physique du Globe de Paris, Paris, France, [4]Department of Earth and Planetary Science, University of California, Berkeley, CA, USA, [5]Laboratoire LULI, Ecole Polytechnique, Palaiseau, France, [6]Geophysical Laboratory, Carnegie Institution of Washington, Washington, DC, USA, [7]Now at Department of Earth and Planetary Sciences, University of California, Davis, CA, USA, [8]Department of Earth and Planetary Sciences, Harvard University, Cambridge, MA, USA, [9]Department of Geophysics and Planetary Sciences, University of Science and Technology of China, Hefei, China, [10]Department of Earth, Atmospheric, and Planetary Sciences, Massachusetts Institute of Technology, Cambridge, MA, USA, [11]Bayerisches Geoinstitut, University of Bayreuth, Bayreuth, Germany, [12]School of Earth Sciences, University of Melbourne, Parkville, Victoria, Australia, [13]Chaire de Physique de l'Intérieur de la Terre, Collège de France, Paris, France, [14]Department of Earth Sciences, University College London, London, UK

**Abstract** Some seismic models derived from tomographic studies indicate elevated shear-wave velocities (≥4.7 km/s) around 120–150 km depth in cratonic lithospheric mantle. These velocities are higher than those of cratonic peridotites, even assuming a cold cratonic geotherm (i.e., 35 mW/m$^2$ surface heat flux) and accounting for compositional heterogeneity in cratonic peridotite xenoliths and the effects of anelasticity. We reviewed various geophysical and petrologic constraints on the nature of cratonic roots (seismic velocities, lithology/mineralogy, electrical conductivity, and gravity) and explored a range of permissible rock and mineral assemblages that can explain the high seismic velocities. These constraints suggest that diamond and eclogite are the most likely high-$V_s$ candidates to explain the observed velocities, but matching the high shear-wave velocities requires either a large proportion of eclogite (>50 vol.%) or the presence of up to 3 vol.% diamond, with the exact values depending on peridotite and eclogite compositions and the geotherm. Both of these estimates are higher than predicted by observations made on natural samples from kimberlites. However, a combination of ≤20 vol.% eclogite and ~2 vol.% diamond may account for high shear-wave velocities, in proportions consistent with multiple geophysical observables, data from natural samples, and within mass balance constraints for global carbon. Our results further show that cratonic thermal structure need not be significantly cooler than determined from xenolith thermobarometry.

## 1. Introduction

Cratons are distinct continental provinces that have been stable since the Archean (e.g., Griffin et al., 2003; Pearson, 1999). They are characterized by thick (≥200 km) lithosphere, as determined from seismic velocities (Jordan, 1975, 1978), surface heat flow (Jaupart & Mareschal, 1999; Morgan, 1984; Nyblade & Pollack, 1993; Rudnick et al., 1998), electrical conductivity (Fullea et al., 2011), and xenolith thermobarometry (Boyd, 1973; Mather et al., 2011; Michaut et al., 2007, 2009). These "cratonic keels" lack a distinct gravity anomaly and thus appear to be in isostatic equilibrium (Perry et al., 2003; Shapiro et al., 1999), and geochemical evidence from peridotitic xenoliths indicates significant chemical depletion by melt extraction (Carlson et al., 2005; Lee, 2003; Lee et al., 2011) that has had a pronounced effect on their density (Schutt & Lesher, 2006). Such observations have led to the concept of a "tectosphere" (Jordan, 1975, 1978), consisting of thick, neutrally buoyant lithosphere that is chemically distinct from the surrounding asthenospheric mantle. Peridotites in these cratonic keels may even be positively buoyant (Poudjom Djomani et al., 2001), in which case their relatively low densities may be balanced by the presence of denser rocks such as eclogite (Kelly et al., 2003). In addition to isostatic contributions to their long-term stability, cratonic keels are likely drier and thus orders of magnitude more viscous than asthenospheric or suboceanic mantle (Hirth et al., 2000; Katayama & Korenaga, 2011; Peslier et al., 2010; Pollack, 1986).

However, cratonic keels are not uniform, as seismic studies have provided evidence for layering and compositional heterogeneity within the cratonic lithosphere. For example, the mid-lithospheric discontinuity
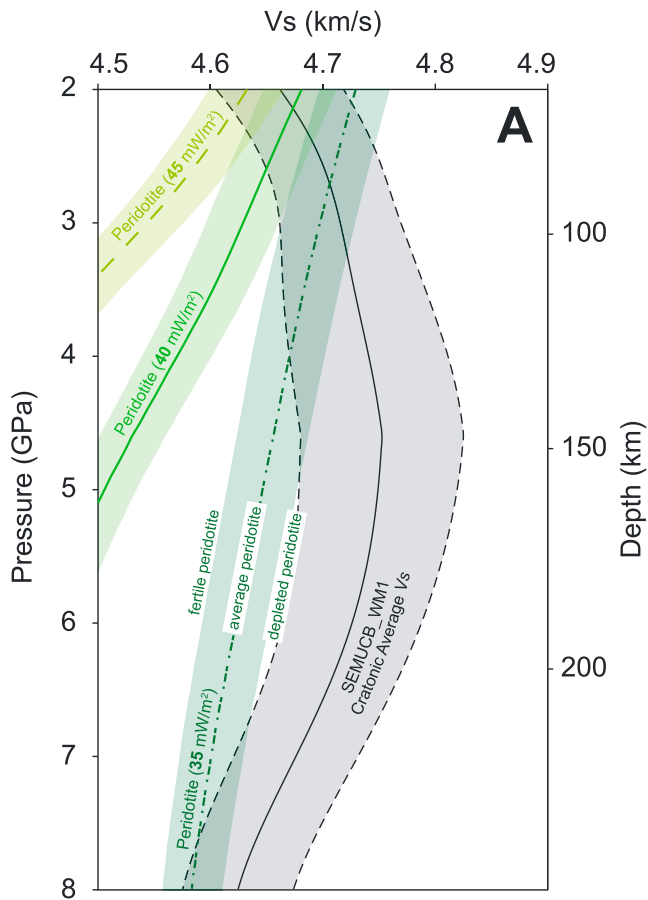
**Figure 1.** Comparison of forward-modeled isotropic and anelastic cratonic peridotite $V_s$ for three steady state conductive geotherms that bracket xenolith *P-T* data (cf. Figure 7); see sections 3 and 4 and Text S1 for methodological details. The data emphasize that cratonic lithosphere requires higher-$V_s$ constituents unless it is composed solely of ~$Fo_{93}$ dunite (i.e., the most melt-depleted known cratonic peridotite composition) *and* has a thermal structure ~100–200 K cooler than measured in xenoliths.

marks the top of a mid-lithospheric low-velocity zone (e.g., Rader et al., 2015; Thybo & Perchuć, 1997) and is also associated with a change in the direction of the fast axis of anisotropy (Yuan & Romanowicz, 2010). Combined with evidence for differences in chemical depletion between the shallower and deeper parts of the lithosphere (e.g., Chesley et al., 1999; Griffin et al., 2003), these data suggest that the cratonic lithosphere consists of several layers that may have been formed or modified by different processes and/or at different times.

These stable cratonic keels exhibit some intriguing seismic properties that are difficult to reconcile with petrologic and geochemical characteristics of cratonic peridotites. Notably, as illustrated here, most global-scale and some continental-scale seismic tomographic models show shear-wave velocities ($V_s$) in excess of 4.7 km/s at depths around 120–170 km in some parts of most cratons at the global scale (Auer et al., 2014; Chang et al., 2015; Debayle et al., 2016; French & Romanowicz, 2014; Lekic & Romanowicz, 2011; Moulik & Ekström, 2014; Schaeffer & Lebedev, 2013) and regional scale (Fichtner et al., 2010; Nita et al., 2016; Yoshizawa, 2014; Zhu et al., 2012). As also illustrated here, these shear-wave velocities are faster than those calculated for any known cratonic peridotite composition, even for the coldest possible cratonic geotherms (James et al., 2004; Lee, 2003) and after accounting for the effect of attenuation on the shear-wave velocities (Bao et al., 2016) (Figure 1; section 2, below). Explaining these velocity excesses thus requires additional mineral or rock constituents with high shear moduli ($G_s$) in cratonic keels. Though there is considerable lithologic heterogeneity observed in xenolith suites (Griffin et al., 2002), only a few potential cratonic materials exhibit significantly faster shear-wave velocities than cratonic peridotite, including eclogite (predominantly due to garnet) and diamond (cf. compilation in Rader et al., 2015).

Here we review evidence for high shear-wave velocities in the cratonic mantle lithosphere by comparing results from different seismic tomography studies of different cratons and confirm the robustness of the high shear-wave velocities with forward modeling of waveforms. We then argue that eclogite and diamond are the most viable candidates that can be added to average peridotite compositions to produce the high shear-wave velocities, and assess heat flow, buoyancy, and electrical conductivity data in concert with phase equilibrium modeling to explore the proportions of eclogite and/or diamond required to produce the high velocities in cratonic keels.

## 2. Statement of the Problem

Many studies have modeled geophysical observations of cratons to understand their compositional and thermal structure (e.g., Afonso et al., 2008; Dalton et al., 2017; Eeken et al., 2018; Hieronymus & Goes, 2010; Hirsch et al., 2015; Jones et al., 2017). These studies reveal disagreement as to how fast cratonic shear-wave velocities are in the depth range ~100–170 km, and whether they can be matched by known cratonic peridotite compositions.

For example, as we will describe further below, many studies that have successfully matched seismologically observed cratonic velocities to peridotite compositions are based on Rayleigh wave dispersion data and do not take into account the presence of significant (2–5%) radial anisotropy in the lithosphere. This approach will underestimate the isotropic shear velocity $V_{siso}$. On the other hand, studies that take into account radial anisotropy, and base their modeling on profiles of $V_{siso}$, have emphasized that the high shear velocity structure beneath cratons cannot be matched solely by peridotite in the depth range ~100–170 km (e.g., Hirsch et al., 2015). Meanwhile, in some cratons (e.g., Kaapvaal craton, South Africa: Jones et al., 2017; and Dharwar craton, India: Maurya et al., 2016), $V_s$ is known to be comparatively low, but these cratons are

small—such that "pure path" estimations of velocities (source-station paths contained entirely within the cra-ton region) are more difficult to obtain, especially at the long periods sensitive to the deeper parts of the lithosphere.

In addition, differences in thermodynamic databases, averaging schemes, bulk compositions, steady state conductive geotherms, and anelastic corrections propagate to significant differences in forward-modeled shear moduli ($G$), density ($\rho$), and $V_s$ for cratonic lithologies. The thermodynamic data sets used for some cal-culations include data and solution models calibrated for crustal conditions (e.g., Holland & Powell, 1998); though the calculated mineral assemblages are similar, equilibrium mineral modes and compositions using such databases may deviate from models calibrated for mantle conditions (e.g., Stixrude & Lithgow-Bertelloni, 2005, 2011). For example, a recent study using the Holland and Powell (1998) thermodynamic data set yields cratonic peridotite $V_s$ ~0.05 km/s faster than the Stixrude and Lithgow-Bertelloni (2005) thermody-namic data set, even though the same shear moduli and averaging schemes (Abers & Hacker, 2016) were used for both calculated mineral assemblages (cf. Eeken et al., 2018, their Figure S2). Further, treating solid-solution end-members as separable phases (Abers & Hacker, 2016; Hacker & Abers, 2004; Hacker et al., 2003) or using Voigt averages for solution-phase shear moduli, as is done in the thermodynamic modeling software Perple_X (Afonso et al., 2008; Connolly & Kerrick, 2002), yield bulk peridotite $V_s$ that can be an additional ~0.05 km/s too fast relative to thermodynamically justified Reuss averages (Stixrude & Lithgow-Bertelloni, 2005; see Text S1). Finally, corrections for anelastic behavior yield significant differences in forward-modeled $V_s$ for a given bulk composition. These corrections are often opaquely described, are based on outdated parameters, or do not match the seismic frequencies for the seismic models to which the velocities are compared.

Figure 1 shows the cratonic average $V_{siso}$ versus depth (and $1\sigma$ range) from a recent global tomographic model (French & Romanowicz, 2014) and calculated shear-wave velocities for fertile, average, and depleted peridotites (Table S1) along a set of steady state conductive geotherms that bracket global cratonic peridotite xenolith P-T conditions (Text S1 and Figure 7). Peridotite $V_s$ was calculated using Perple_X free energy mini-mization software (Connolly, 2009), thermodynamic data, solution models, and shear moduli from Stixrude and Lithgow-Bertelloni (2005, 2011), and temperature, frequency (1 Hz), and grain-size (1 cm) sensitive attenuation corrections from Jackson and Faul (2010). (Calculation details are discussed in sections 3 and 4 below and in the supporting information.) Figure 1 illustrates the problem addressed by this study: using state-of-the-art seismological and forward-modeling parameters, even the most depleted peridotites along the coolest possible steady state conductive geotherms matching xenolith P-T data cannot explain the observed global cratonic average $V_s$ in this tomographic model. Since this tomographic model is arguably on the fast side of the ensemble of available shear velocity models, in the next sections, we consider different seismological models to evaluate a range of representative cratonic $V_s$ profiles, and perform robust forward modeling of different lithologies to try to explain the consistently fast $V_s$ found in some parts of cratons in the depth range 100–170 km.

## 3. Seismological Constraints

There is significant variability in shear-wave velocity versus depth profiles among different seismic tomographic models, which may be due to a combination of factors: differences in (1) the theoretical assumptions on seismic wave propagation in a 3-D Earth, (2) accounting (or not) for seismic anisotropy, especially radial anisotropy, which is known to be prevalent in the upper mantle and particularly in continents (e.g., Babuška et al., 1998; Dziewonski & Anderson, 1981; Gung et al., 2003; Lebedev et al., 2009; Montagner & Tanimoto, 1991; Nataf et al., 1984), (3) how crustal structure is accounted for in the tomographic inversion, and/or (4) how regularization and smoothing affects the resulting velocity-depth profiles. Notably, most previous studies dedicated to explaining seismic observations in terms of mineralogy and associated geotherms have relied either on fitting observed phase velocity dispersion curves for Rayleigh waves (e.g., Darbyshire & Eaton, 2010; Eeken et al., 2018; Jones et al., 2017), or on shear velocity models that were derived from Rayleigh wave dispersion observations (e.g., Bruneton et al., 2004). However, Rayleigh waves are polarized in the vertical plane; thus, they are sensitive to $V_{sv}$ rather than $V_{siso}$. In the lithosphere, the velocity of shear waves polarized horizontally ($V_{sh}$) is a few percent larger than $V_{sv}$, which is diagnostic of radial anisotropy and is captured by $\xi > 1$, where $\xi = (V_{sh}/V_{sv})^2$, the anisotropic parameter to which surface waves are most sensitive. Thus, models based exclusively on Rayleigh waves may underestimate the

isotropic shear velocities. For lithospheric studies constrained by surface wave and overtone observations—and in order to access the Voigt average isotropic shear velocity, which can be approximated by $V_{siso}^2 \sim (V_{sh}^2 + 2V_{sv}^2)/3$—it is necessary to include observations on the transverse component of motion, which contain horizontally polarized Love waves and their overtones. Notably, most studies based on surface wave dispersion data apply approximate crustal corrections, which may introduce biases in the estimation of radial anisotropy in the uppermost mantle (Ferreira et al., 2010; Lekić et al., 2010), and therefore the estimation of isotropic shear velocities. Finally, most models constrained by surface wave data, whether based on dispersion data or seismic waveforms, are based on the "path average approximation," which averages the structure between the source and the receiver in a way that is powerful but not rigorously correct, especially for Love waves (e.g., Mégnin & Romanowicz, 1999), and may not allow the accurate resolution of $V_{siso}$ amplitude in regions of small lateral extent, such as the deep roots of some cratons.

Thus, it is necessary to evaluate and quantify the variability across models and determine which type of model provides better fits to observed seismic waveforms, which represent the "raw" seismic data, before any inversion process. For the synthetic calculation of the predicted seismic wavefield in any given model, we take advantage of the spectral element method (SEM), which involves a purely numerical integration of the equations of motion (e.g., Komatitsch & Tromp, 1999; Komatitsch & Vilotte, 1998), makes no theoretical simplifying assumptions, and has been shown to provide accurate predictions of the seismic wavefield in arbitrary 3-D Earth structure. To assess model fits, we have computed synthetic seismograms in several tomographic models that exhibit large differences in their shear velocity profiles, and compare them to observed three-component waveforms. The chosen paths, as we will describe below, can be considered as "pure paths," that is, contained entirely within a cratonic region.

To extract shear velocity profiles that are representative of cratonic areas with deep lithospheric roots (>150 km), one can proceed in several ways. One is based on the geological information on the age of the crust. However, there is not a one-to-one correspondence between the age of crust and thickness of the lithosphere, with some cratons having clearly lost their deep roots, for example, the North China craton (e.g., Chen, Cheng, et al., 2009), or the eastern part of the Superior Craton in north America (Clouzet et al., 2018; Darbyshire et al., 2013). A more objective classification of lithospheric provinces can be done through cluster analysis of upper mantle shear velocity models (Lekic & Romanowicz, 2011). In such an analysis, $V_{siso}$ profiles as a function of depth are first extracted from a given model on a 2° × 2° grid on the Earth's surface, for the depth range 50–300 km, and then these profiles are classified into N families of statistically similar velocity profiles using k-means cluster analysis (MacQueen, 1967). The distance between two $V_{siso}$ vectors (i.e., $V_{siso}$ sampled in depth beneath a particular location on the Earth's surface) is quantified using the standard L2-norm. As shown in Lekic and Romanowicz (2011) at the global scale, the signature of cratons is clearly distinct from that of other regions for $N \geq 6$ and is independent of any geological bias based on crustal ages.

Figure 2 shows the results of such a cluster analysis of the upper mantle isotropic velocity structure ($V_{siso}$) in four recent global radially anisotropic shear-wave velocity models, developed using different methodologies and data sets. While model SEMUCB_WM1 (French & Romanowicz, 2014) exhibits the fastest velocities, in all of these models, the average shear-wave velocity in the craton cluster reaches or exceeds 4.7 km/s at some depths between 100 and 170 km. The 1σ and 2σ standard deviation bands show that in some areas, $V_{siso}$ even exceeds 4.8 km/s. Two other recent global $V_{sv}$ models (Figure S1) also show high $V_{sv}$ between 120 and 160 km, providing lower bounds for $V_{siso}$. An exception is model ND08 (Nettles & Dziewonski, 2008), for which the cratonic $V_{siso}$ profile shows the highest velocities at shallow depth. We note however, that there are also large differences between the ξ profiles in the cratonic regions of the seven models analyzed (Figure S2).

We further explored the variability of the shear-wave velocity versus depth profiles in several cratons by comparing profiles from cluster analyses of global tomographic models with those obtained from continental-scale regional models (Fichtner et al., 2010; Kennett et al., 2013; Nita et al., 2016; Priestley et al., 2008; Sebai et al., 2006; Yoshizawa, 2014; Yuan et al., 2014; Zhu et al., 2012; see Figures S3–S6). In each case, we used k-means cluster analyses to extract the craton regional boundaries, and determined the average shear-wave velocity within each craton. For the regional models, we used $N = 4$, as this choice of N provides robust regional boundaries and consistent average $V_s$ profiles. The choice of N for the regional models is smaller than for the global models because the regional models lack oceanic regions included in the global models. This analysis shows that there are large differences (up to ±5%) between models in the depth range
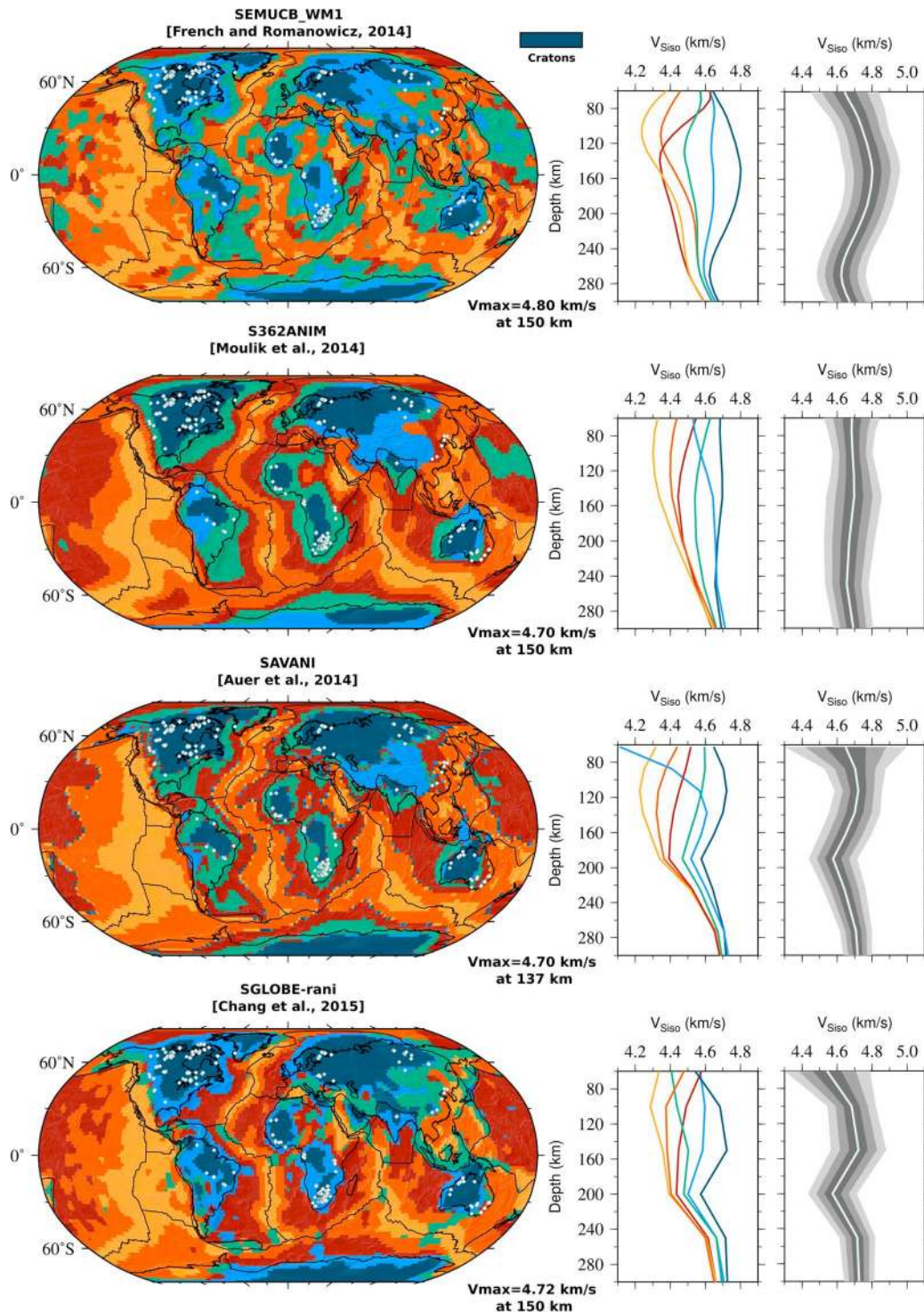
**Figure 2.** Cluster analysis (*N* = 6) of $V_{siso}$ in radially anisotropic global models SEMUCB_WM1 (French & Romanowicz, 2014), S362ANI + M (Moulik & Ekström, 2014), SAVANI (Auer et al., 2014), and SGLOBE_rani (Chang et al., 2015) in the depth range 60–300 km, revealing cratons with faster than average $V_S$ down to at least 180 km depth (dark blue regions and associated colored velocity profiles on the right of each map). Note that Tibet and Altiplano are singled out as regions of lower than average velocities at shallow depth, but similar to cratons below 200 km depth in model SEMUCB_WM1. Diamonds are found primarily on the edges of cratons and are shown as white dots (from the compilation of Faure, 2010). In all four models, the three oceanic regions show the age progression of the oceanic lithosphere (yellow to brown), and the cratonic regions (dark blue) have comparable geographic extents. There is more variability in the clustering results for the two other continental clusters that come out of the analysis (green and light blue). The grey shaded panels on the right show the average $V_{siso}$ profile in the cratonic region in each model (white line), surrounded by 1σ, 2σ, and 3σ bands (black to light grey). All models show velocities in excess of 4.7 km/s between 100 and 170 km depth in at least some parts of some cratons (see also Figure 3). The results of a similar analysis for three other global models are shown in Figure S1.
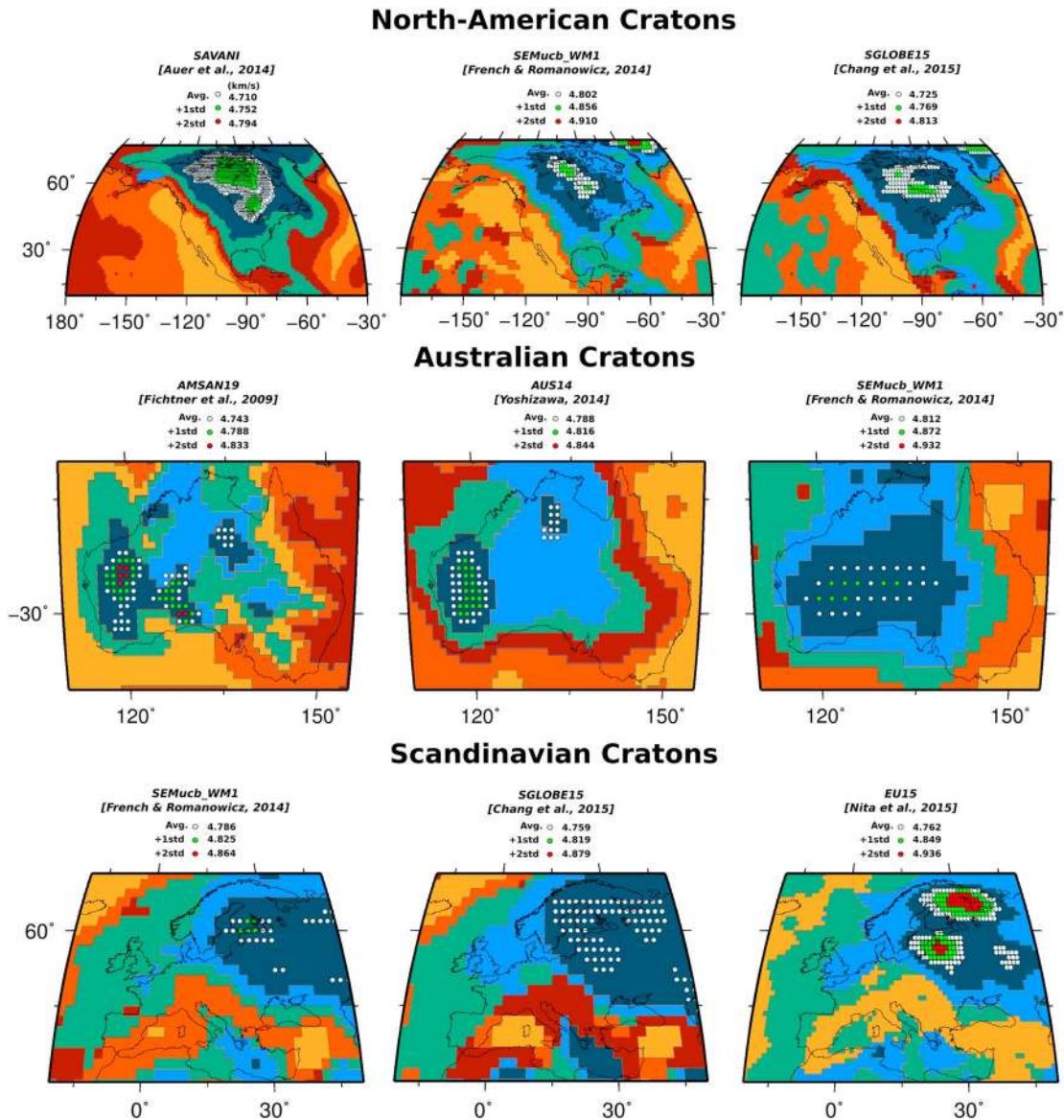
**Figure 3.** Distributions of $V_{siso}$ as obtained from cluster analysis in (top) North America and (bottom) Australia. The colors are as in Figure 2, with cratonic regions in dark blue. The white dots within the cratonic regions indicate locations where the $V_{siso}$ profile is faster than the average for the cratonic region in the depth range 100–150 km, but within 1σ of that average. The green (resp. red) dots indicate locations where those velocities are between 1σ and 2σ of the average (resp. between 2σ and 3σ). Models shown are global models SEMUCB_WM1 (French & Romanowicz, 2014), SAVANI (Auer et al., 2014), and SGLOBE_rani (Chang et al., 2015) for North America, and SEMUCB_WM1, as well as two regional models: AMSAN19 (Fichtner et al., 2010) and AUS14 (Yoshizawa, 2014). Compared to global model SEMUCB_WM1, the regional models in Australia provide a refined view of the cratonic structure, with more localized fast velocities, generally consistent with the geological extent of cratons: in particular Slave and Rae cratons in North America, and Pilbara and Yilgarn cratons in Australia (corresponding tectonic maps are not shown but can be found, for example, in Whitmeyer and Karlstrom, 2007, for North America or Yoshizawa, 2014, for Australia).

of interest (100–170 km) in all the cratons shown, both in $V_{sv}$ (for models constructed using only vertical component data) and $V_{siso}$ (for models constructed using three-component data and including radial anisotropy)—likely due to a combination of methodology and data sets considered. While the average cratonic profiles in SEMUCB_WM1 (French & Romanowicz, 2014) are consistently on the fast side, other regional models also exhibit average $V_{siso}$ faster than 4.7 km/s in the relevant depth range (e.g., multiple cratons in North America, Australia, and the Baltic Shield).

To further assess the robustness of the fast velocities within some well-studied cratons, Figure 3 shows the geographical distribution of the $V_{siso}$ profiles that are 1-2σ faster than the cratonic average $V_{siso}$ determined by cluster analysis of the corresponding model. These velocity deviations were calculated for the depth range
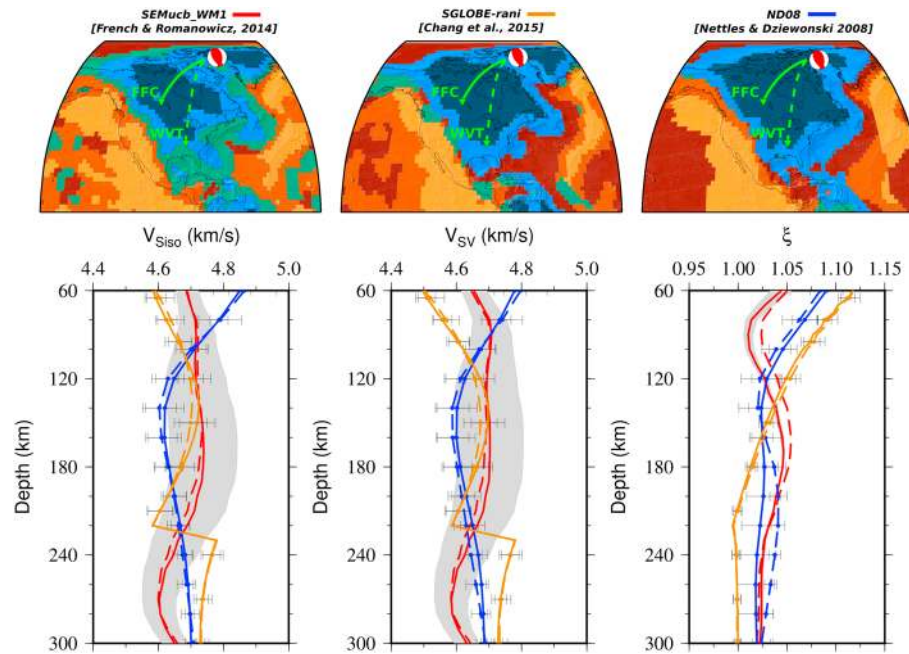
**Figure 4.** Comparison of predicted velocity and anisotropy profiles for three radially anisotropic shear-wave models and for two "pure paths" across the North American craton. (top row) Regionalized maps of North America from cluster analysis with $N = 4$, for models (left) SEMUCB_WM1 (French & Romanowicz, 2014), (middle) SGLOBE_rani (Chang et al., 2015) and (right) ND08 (Nettles & Dziewonski, 2008), showing the two paths considered. (bottom) Comparison of average depth profiles of shear-wave velocity (left) $V_{siso}$, (middle) $V_{sv}$, and (right) anisotropic parameter $\xi$ in the three models, along the paths from the event in Baffin Bay to station FFC (continuous lines) and WVT (dashed lines). Red: SEMUCB_WM1; blue: ND08; orange: SGLOBE_rani. The grey band shows the range of velocities in model SEMUCB_WM1 for the North American craton cluster (dark blue in top panels), while the standard deviation for the craton clusters in the other two models are indicated by horizontal bars.

100–150 km for several models of North American and Australian cratonic regions. Interestingly, the distributions are not random, but delineate contiguous high-$V_s$ regions that are increasingly smaller in size and centered toward the interior of the cratons, depending on lateral resolution of the model. This indicates consistency among some models, in which the fastest velocities correspond to a geographically limited area within the cratons. As shown in Figure S7 for North America, not all models show such a coherent pattern, and some are clearly smoother, but all except ND08 exhibit extended regions within the craton with velocities exceeding 4.7 km/s in the depth range 100–150 km.

The differences between models may be due to the level of regularization applied in the inversion process or the theory used for 3-D seismic wavefield computations: path-average approximation using normal mode summation in most cases versus more accurate SEMs in the case of SEMUCB_WM1 (French & Romanowicz, 2014) and EU30 (Zhu et al., 2012), which show similarly fast $V_{siso}$ in the Scandinavian shield (Figure S4). The differences may also be due to the way crustal structure is accounted for, which can have an influence on the retrieved mantle structure (Ferreira et al., 2010; Lekić et al., 2010); some groups apply crustal corrections based on existing crustal models (ED16, SL13, and ND08), others model crustal effects using SEM on an existing crustal model (AuSREM and EU30), and others fit short-period dispersion data (SEMUCB and EU15). Though determining the cause of the discrepancies is beyond the scope of this study, we note that profiles obtained by simultaneous transdimensional Markov chain Monte Carlo modeling of fundamental mode Rayleigh wave dispersion and converted $P$-to-$S$ phases—that is, studies in which the crustal and lithospheric structures are simultaneous modeled—also obtain $\geq 4.7$ km/s $V_{sv}$ values at ~150 km depth beneath stations located in the North American cratons (e.g., Bodin et al., 2016; Calò et al., 2016).

To determine which models best fit the observed seismograms, we considered the case of North American cratons, which are well sampled by seismic paths and for which it is possible to consider source-station paths that are contained within the cratonic region (i.e., "pure paths"). We compared the predictions of three
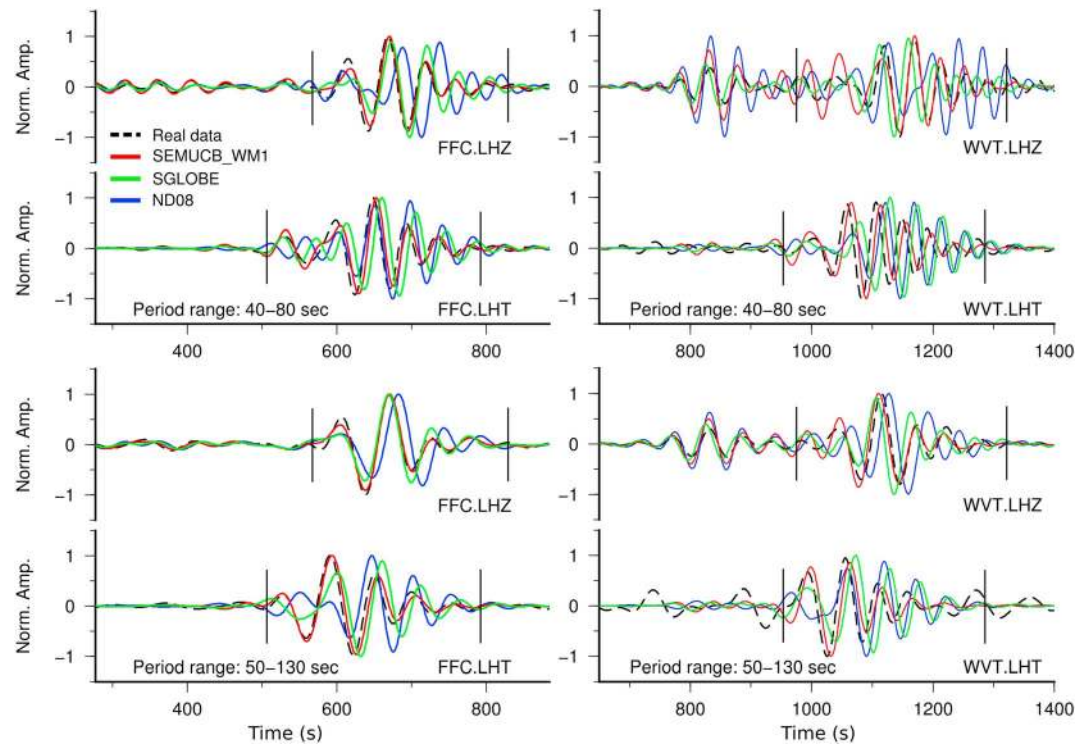
**Figure 5.** Comparison of observed and synthetic waveforms at station (left) FFC and (right) WVT in two different period bands: (top) 40–80 s and (bottom) 50–130 s. Each panel shows the comparison on the vertical component (LHZ) and the transverse component (LHT). The data are shown in a black dashed line, the predictions for model SEMUCB_WM1 in red, the predictions for model SGLOBE in green, and those for model ND08 in blue. In all cases, the predictions from model SEMUCB_WM1 generally fit the data best both in phase and in amplitude. Notably, the Z component predictions are systematically too slow for model ND08. The quality of fits for model SGLOBE is intermediate.

radially anisotropic models with contrasting properties on two such pure paths (Figure 4): (i) a model showing particularly slow velocities in the depth range 100–200 km (ND08: Nettles & Dziewonski, 2008), developed using asymptotic normal mode perturbation theory (the "path-average approximation"); (ii) a model showing particularly fast velocities in that same depth range (SEMUCB_WM1: French & Romanowicz, 2014), developed using the SEM for 3-D wavefield computations; and (iii) a model with intermediate $V_{siso}$ values (SGLOBE_rani: Chang et al., 2015), which used the path-average approximation but allowed for crustal thickness perturbations. We chose data from a 2010 earthquake in Baffin Island that was not used in the construction of model SEMUCB_WM1, and two paths that are entirely within the craton (Figure 4, top row) as defined from the cluster analysis for each of the three models. Figure 4 (bottom row) shows a comparison of the average and standard deviation of $V_{siso}$ and $\xi$ along each path as a function of depth in the upper mantle and indicates significant differences between the three models in different depth ranges. ND08 is faster than the other two models down to 90 km depth, and slower in the 120–180 km depth range where SEMUCB_WM1 and SGLOBE_rani are in good agreement. At shallower depths, the differences appear to be compensated by differences in the anisotropic $\xi$ parameter, while in the deeper depth range—of interest in this study—the differences in $\xi$ are less pronounced among the three models.

We further compared the synthetic waveforms predicted for the two modeled paths to observed waveforms on the vertical (Z: sensitive to $V_{sv}$) and transverse (T: sensitive to $V_{sh}$) components in two frequency bands (40–80 s and 50–130 s; Figure 5). The synthetics were computed using RegSEM (Cupillard et al., 2012), which is a continental-scale version of a numerical wavefield simulation code based on the SEM. RegSEM includes the effects of sphericity, radial anisotropy, and attenuation, as well as absorbing lateral boundaries (perfectly matched layers) to account for the finite boundaries of the region considered. As Figure 5 illustrates, the synthetic fundamental mode waveforms match the data significantly better for the faster upper mantle model (SEMUCB_WM1) than for the slower one (ND08) in both frequency bands. The vertical component
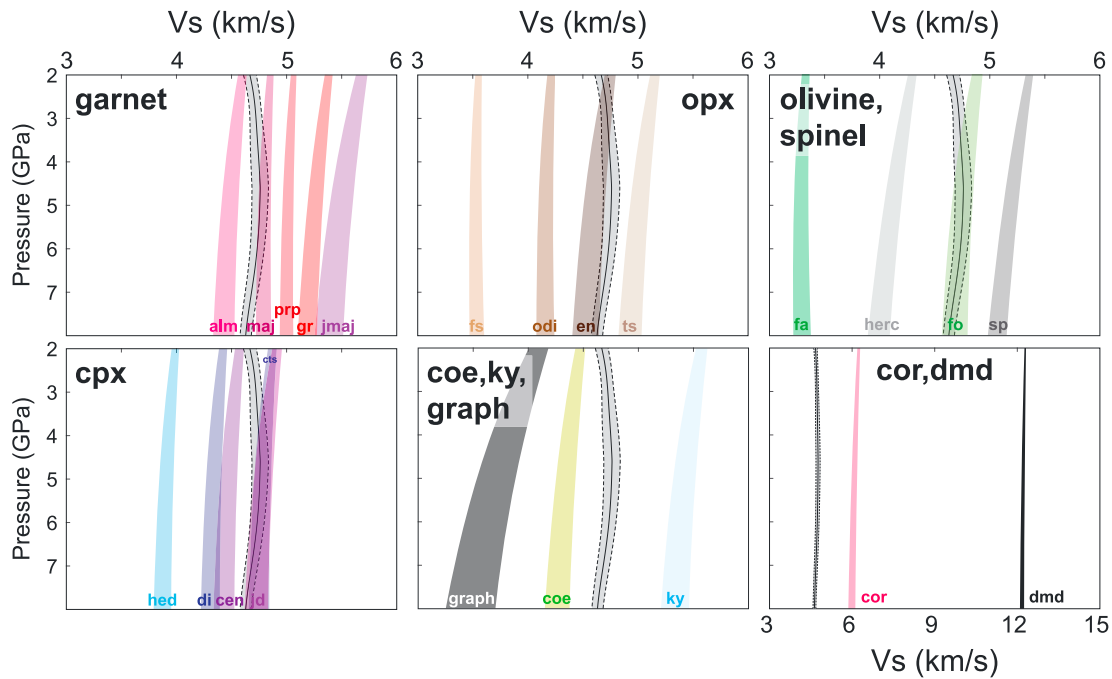
**Figure 6.** Calculated $V_s$ profiles for mantle mineral end-members and pure phases along cratonic geotherms, plotted with the SEMUCB_WM1 (French & Romanowicz, 2014) average cratonic $V_s$ from the cluster analysis in this study (solid black curve bounded by gray shading and outlined with black dashed lines). The profiles are shown over the entire depth range of interest, that is, without regard for the stability field of each end-member; see text for modeling details. The colored regions span the $V_s$ for each end-member or phase along the three geotherms shown in Figure 7, with the fastest velocities corresponding to the coolest geotherm. Note (i) the difference in scale for the corundum and diamond results and (ii) that $G_s$ for a solution phase constructed from these end-members is a Reuss average, not a Voigt average. Mineral abbreviations are as follows: alm = almandine, maj = majorite, prp = pyrope, gr = grossular, jmaj = Na-majorite, fs = ferrosilite, odi = orthodiopside, en = enstatite, ts = NaAl-orthopyroxene, hed = hedenbergite, di = diopside, cen = clinoenstatite, jd = jadeite, fa = fayalite, fo = forsterite, herc = hercynite, sp = spinel, coe = coesite, ky = kyanite, graph = graphite, cor = corundum, dmd = diamond.

(LHZ) synthetics show that the ND08 $V_{sv}$ model is too slow (by almost a quarter period) at both stations and in both frequency bands, while those for SEMUCB_WM1 match the data significantly better in both phase and amplitude. For the transverse component (LHT) waveforms, the match between observed and synthetics is best for SEMUCB_WM1, although the match in phase is good for ND08 in the early part of the Love wave. SEMUCB_WM1 synthetics match the later parts of the waveforms better than the other models (e.g., after 700 s for station FFC and after 1100 s for station WVT), although they are slightly too slow. The fits for SGLOBE_rani synthetics are better than those for ND08 for the early part of the Rayleigh and Love waveforms, that is, the longer periods that are sensitive to the depth range of interest here (120–180 km), where SGLOBE and SEMUCB_WM1 agree on the presence of high shear-wave velocities. Still, SGLOBE predicts slightly later arrivals than SEMUCB on the $T$ component in both frequency bands and at both stations.

Because the 3-D synthetics computed using SEMUCB_WM1 most accurately predict the seismic wavefield, we infer that—at least in some parts of cratons (see Text S2), and at depths around 150 ± 30 km—$V_{siso}$ is indeed ≥4.65–4.7 km/s. In the following section, we aim to fit these velocity profiles with mineralogy and thermal structure.

## 4. Mineralogical and Petrological Constraints

### 4.1. Constituents With High Shear Moduli

To determine the mineral or rock constituents responsible for the observed high shear-wave velocities ($V_s$), we calculated end-member mineral $V_s$ (Figure 6) over the pressure-temperature ($P$-$T$) range of interest using the free-energy minimization software Perple_X (Connolly, 2009) with the thermodynamic data set of Stixrude and Lithgow-Bertelloni (2005, 2011). Figure 6 shows a variety of candidate mineral end-members that meet or exceed the SEMUCB_WM1 high $V_s$ calculated along cratonic geotherms (Text S1 and Figure 7). Diamond has the fastest $V_s$ (~12 km/s), and other mineral end-members with high $V_s$ are aluminous orthopyroxene, jadeite,
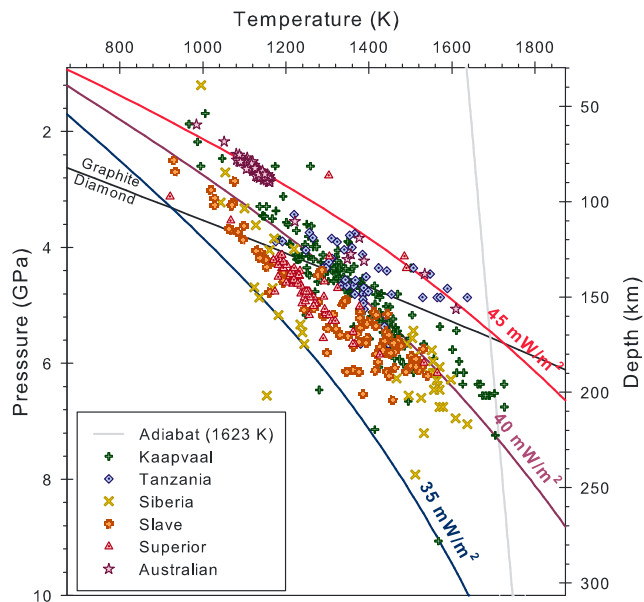
**Figure 7.** Comparison of pressure-temperature conditions estimated from kimberlite-hosted garnet peridotite xenoliths (Data Set S2), with the modeled geotherm range calculated for different surface heat flows labeled in mW/m², and the diamond-graphite phase boundary (Day, 2012). Xenolith data from the Siberian craton (Canil et al., 1994; Ionov et al., 2010; Yaxley et al., 2012), the Slave craton (Kopylova et al., 1999; McCammon & Kopylova, 2004; Creighton et al., 2010), the Kaapvaal craton (Boyd et al., 1993; Canil et al., 1994; McCammon et al., 2001; Woodland & Koch, 2003; Creighton et al., 2009; Lazarov et al., 2009; Woodland, 2009), the Superior craton (Meyer et al., 1994; Hunt et al., 2012), the Tanzanian craton (Rudnick et al., 1994; Lee & Rudnick, 1997; Koornneef et al., 2009; Gibson et al., 2013), and the Gawler craton in Australia (Tappert et al., 2011) are contained in Data Set S2. See Text S1 for additional details.

kyanite, corundum, Mg-spinel, and most garnet end-members—all of which exceed the observed cratonic average $V_s$. Because garnet, jadeite, and kyanite are all common phases in eclogites (jadeite forms a solid solution with diopside and hedenbergite to make omphacite), it follows that eclogite may also explain the high observed $V_s$.

Determining which rocks or minerals are responsible for the high $V_s$ also requires understanding their occurrence in the depth interval of interest. The most direct geochemical knowledge of cratonic mantle lithosphere comes from kimberlite magmas that carry mantle xenoliths and diamonds to Earth's surface. These xenoliths are dominated by peridotites (Boyd, 1989; Nixon, 1987; Nixon et al., 1981; Pearson et al., 2003) that likely originate from the Moho to >200 km depths (Figure 7). Eclogite xenoliths are typically less abundant than peridotite, but are locally enriched in some kimberlites (e.g., Jericho kimberlite, Slave craton: Kopylova et al., 1999; and Roberts Victor kimberlite, Kaapvaal craton: Pearson et al., 2003); the abundance of eclogite xenoliths may not be directly proportional to their actual lithospheric abundances, but could reflect a sampling bias of the particular kimberlite, or preferential preservation of certain lithologies. Using garnet chemistry and abundance from multiple eclogite-rich kimberlite concentrates, Schulze (1989) calculated that eclogites constitute less than 2 vol.% of the cratonic upper mantle; analyses from the Slave craton yielded similar results of <4 vol.% (McLean et al., 2007) and ≪10 vol.% eclogite (Griffin, Doyle, et al., 1999). Other nonperidotitic xenoliths—including pyroxenites and mica- and amphibole-rich rocks—are also observed, but are typically much less abundant than peridotite and eclogite (Boyd & Gurney, 1986; Pearson et al., 2003).

Diamonds are also brought to the surface by kimberlite magmas and are typically found as xenocrysts in the kimberlite matrix or within eclogite xenoliths. Interestingly, diamonds are less commonly found in peridotitic xenoliths (Boyd & Finnerty, 1980; Jaques et al., 1990; Thomassot et al., 2007; Viljoen et al., 1992, 2004), potentially due to the breakdown of diamond-bearing peridotite xenoliths during kimberlite infiltration/metasomatism and ascent (Schulze, 1989; Shirey et al., 2013). Graphite pseudomorphs after diamond have also been found in massif peridotites, for example, in garnet pyroxenite layers in the Beni Bousera peridotite massif in Morocco (Pearson et al., 1989) and in the Ronda peridotite in southern Spain (Davies et al., 1993). As estimated from thermobarometry of their silicate inclusions, most kimberlitic diamonds (~90%: Stachel & Harris, 2008) formed in the mantle lithosphere between ~4.3 and 8.3 GPa ($T \approx$ 1153–1673 K); inclusion suites further indicate that ~64% of diamonds are peridotitic (especially harzburgitic) and ~33% are eclogitic in origin (Stachel & Harris, 2008). Diamond concentrations in kimberlite-borne xenoliths are generally low (<0.0001–0.01 vol.%; Pearson et al., 2003), but some peridotite and eclogite xenoliths contain concentrations up to 0.02–0.5 vol.% and >2 vol.% diamond, respectively, with some xenoliths exhibiting diamond-rich "seams" (Anand et al., 2004; Schulze et al., 1996; Viljoen et al., 1992, 2004).

Though we cannot exclude the presence of additional mineralogical or petrological components or phases responsible for the observed high cratonic shear-wave velocities (see Text S3 for discussion; cf. Aulbach & Jacob, 2016; Bass, 1986; Frost & McCammon, 2008; Isaak & Ohno, 2003; Klemme et al., 2009; McCammon, 2005; Milman et al., 2001; Reichmann et al., 2013; Stagno et al., 2013; Ziberna et al., 2013; Ziberna & Klemme, 2016), we note that (i) eclogitic minerals (garnet, omphacite, and kyanite) and diamond have the highest $V_s$ of commonly observed cratonic mantle constituents in xenoliths, (ii) both are key constituents of erupted mantle material from subcratonic lithospheric mantle over the depth range of interest in this study, and (iii) their bulk abundances in cratonic lithospheric mantle are loosely constrained.

## 4.2. Thermodynamic and Mixing Models: Methods Summary

Complete method details are contained in Text S1. We used Perple_X Gibbs free energy minimization software (Connolly, 2009) to calculate shear-wave velocity profiles through the cratonic lithosphere for peridotite,
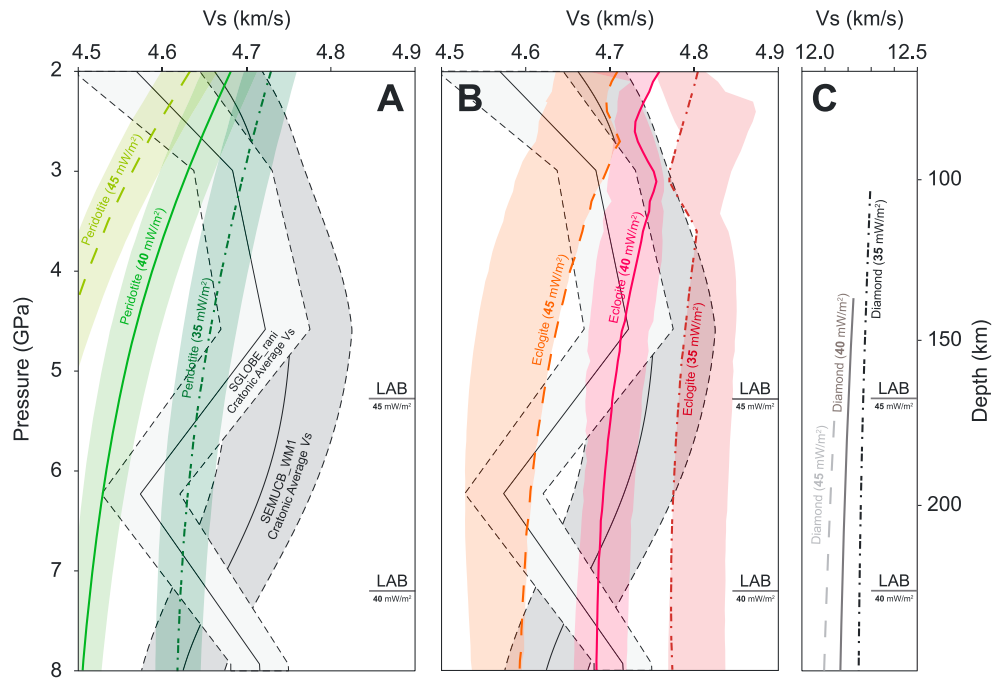
**Figure 8.** $V_s$ profiles for end-member cratonic peridotite, eclogite, and diamond; see also Data Set S3. 1σ velocity uncertainties are 1–2%, but absolute values depend on mineral assemblage (Stixrude & Lithgow-Bertelloni, 2005). (a) Cratonic peridotite shear-wave velocity ($V_s$) calculated for three different geotherms (green shaded regions), compared to the average cratonic $V_s$ profiles determined using cluster analyses on seismic tomography models SEMUCB_WM1 (darker gray) and SGLOBE_rani (lighter gray). The velocities are not corrected for temperature and grain-size sensitive anelastic behavior (Faul & Jackson, 2005; Jackson & Faul, 2010) and thus are maxima. As in Figure 1, shaded regions do not represent 2σ error bounds, but rather identify $V_s$ ranges calculated for different peridotite compositions; lines reflect "average" peridotite compositions (Table S1). "LAB" identifies the lithosphere-asthenosphere boundary (defined in the main text) for the two hottest geotherms shown in each figure, whereas the LAB for the coolest geotherm (35 mW/m$^2$) is deeper than the extent of the figure. (b) Cratonic eclogite shear wave velocity profiles for the same geotherms as in (a), uncorrected for anelastic behavior. Note that the broad shaded regions are not symmetric about the "average" eclogite $V_s$ because (i) cratonic eclogite compositions are more compositionally heterogeneous than peridotite and (ii) alternative bulk compositions pass through $P$-$T$ fields with different mineral assemblages, distinct mineral compositions, and thus variable bulk rock shear moduli. (c) Diamond $V_s$ for the same geotherms as in (a) and (b), uncorrected for anelastic behavior. Each line is restricted to the diamond stability field specific to that geotherm, after Day (2012) (cf. Figure 7, this paper); at shallower depths, graphite ($V_s$~4.0 km/s; cf. Figures 6 and 9, this paper) is stable.

eclogite, and diamond, using silicate and oxide thermodynamic data and solution models from Stixrude and Lithgow-Bertelloni (2005, 2011), diamond data from Valdez et al. (2012), and graphite data from Holland and Powell (1998, and references therein). Bulk compositional data for cratonic peridotite and eclogite xenoliths in kimberlites were assembled from PetDB (Lehnert et al., 2000), GEOROC (http://georoc.mpch-mainz.gwdg.de), and additional studies (Aoki & Kushiro, 1968; Danchin, 1979; Ehrenberg & Griffin, 1979; Hills & Haggerty, 1989; Ionov et al., 2010; Jacob & Foley, 1999; Jacob et al., 2003; Jacob et al., 2009; Nehru & Reddy, 1989; Pyle & Haggerty, 1998; Rudnick et al., 1998; Schmickler et al., 2004; Shervais et al., 1988; Sobolev, 1977; Taylor & Neal, 1989; see Figure S8, Text S1, and Data Set S1). We calculated global average "maximum," "minimum," and "average" peridotite and eclogite compositions—defined relative to MgO—to assess the role of compositional heterogeneity in our results (Table S1); mineral modes for each are shown in Figure S9. Steady state cratonic geotherms for calculation of equilibrium mineral assemblages were modeled with different surface heat flow ($Q_0$) values (35, 40, and 45 mW/m$^2$) that further bracket global kimberlite xenolith thermobarometry data (Figure 7); geotherms were calculated after Pollack and Chapman (1977), Chapman (1986), and Rudnick et al. (1998) with thermal conductivity of mantle lithosphere calculated after Schatz and Simmons (1972). The mantle adiabat (Figure 7) was constructed with a potential temperature of ~1623 K and a thermal gradient of 0.4 K/km. Adiabatic shear moduli ($G_s$) for each bulk-rock composition were assembled in two steps: moduli for each solution phase were corrected to a Reuss average of end-member moduli rather than the raw Perple_X output Voigt average (cf. Figure S10), after which the bulk-
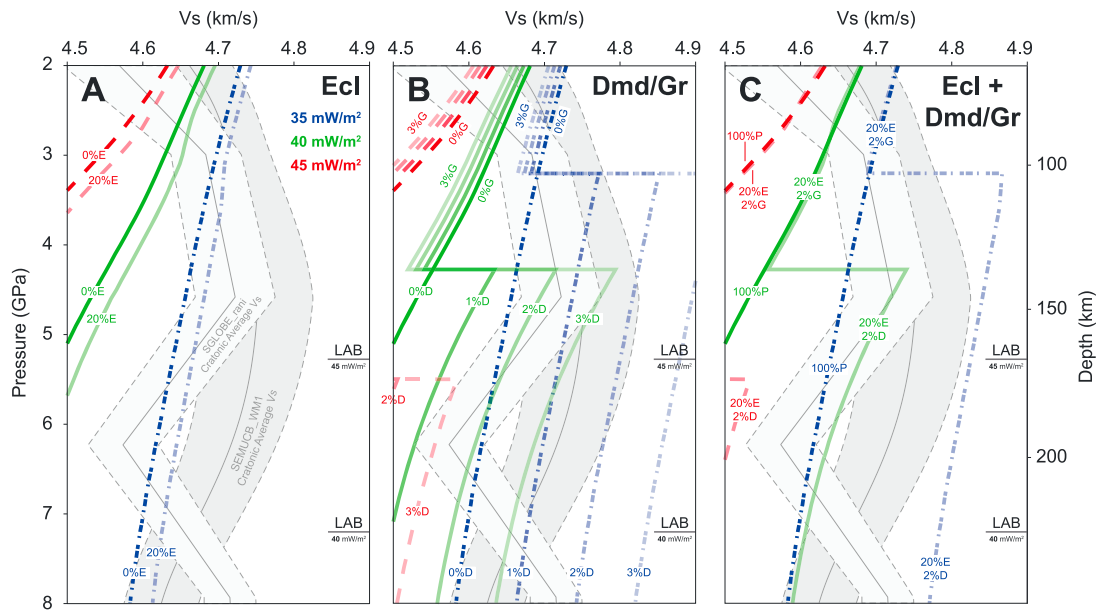
**Figure 9.** Results of peridotite ± eclogite ± diamond mixing models. See Text S1 for details of the mixing calculations, Figure 8 for individual, anharmonic lithologic $V_s$ profiles, and Data Sets S4–S9 for anharmonic (elastic) velocities. All profiles are corrected for anelasticity with a 1 s period and 1 cm grain size (Jackson & Faul, 2010; Data Set S10), and are shown for the compositional "average" peridotite and eclogite (Figure S8; Table S1). Calculated $V_s$ profiles from two shear-wave tomographic models are shown in each figure as gray shaded fields; note that these models are referred to 1 s periods, that is, identical to the anelasticity correction. In each panel, mixing results for the coolest geotherm that brackets xenolith thermobarometry (cf. Figure 7) are shown in blue dashed-dotted lines (35 mW/m²), results for the intermediate geotherm are shown in green solid lines (40 mW/m²), and results for the hottest geotherm are shown in red dashed lines (45 mW/m²). (a) Two-component peridotite + eclogite mixing model results; only 20 vol.% eclogite is shown to account for neutral buoyancy constraints. (b) Results of two-component peridotite + graphite/diamond mixing models, with the position of the graphite to diamond transition determined by the geotherm (see text) and data from Day (2012). (c) Results of three-component peridotite + eclogite + diamond mixing models, showing the effect of combining ~20 vol.% eclogite with ~2 vol.% diamond or graphite.

rock $G_s$ was calculated as a Voigt-Reuss-Hill average of all solution phases. Anharmonic $V_s$ (i.e., not corrected for anelasticity) calculated for peridotite, eclogite, and diamond using these methods is shown in Figure 8; 1σ velocity uncertainties are 1–2%, but absolute values depend on mineral assemblage (Stixrude & Lithgow-Bertelloni, 2005). Using the end-member lithologic $G_s$ and density data, and applying a correction for anelastic mineral behavior (Faul & Jackson, 2015; Jackson & Faul, 2010), we forward-modeled mechanical mixtures of each lithology that could explain the average cratonic $V_s$ profiles in models SEMUCB_WM1 (French & Romanowicz, 2014) and SGLOBE_rani (Chang et al., 2015; Figure 9). Models with diamond include graphite at depths shallower than the diamond-graphite transition.

### 4.3. Thermodynamic and Mixing Models: Results

The calculated vol.% eclogite (Figure 9a) and/or diamond (Figure 9b) required to match the $V_s$ profiles depends primarily upon (i) the peridotite and eclogite compositions and (ii) the geotherm. Additionally, though velocities shallower than ~100 km are not affected, accounting for anelastic behavior becomes increasingly important with depth and is more significant for hotter geotherms (e.g., compare anharmonic peridotite in Figure 8a versus anelastic peridotite in Figure 9a). For two-component peridotite + eclogite mixtures, >50 vol.% eclogite is required to match the SEMUCB_WM1 $V_s$ profile when surface heat flow $Q_0 = 35$ mW/m², and even 100 vol.% eclogite cannot match this $V_s$ for $Q_0 = 40$–45 mW/m². Lesser but still significant fractions of eclogite are required to match the highest-$V_s$ portions of the SGLOBE_rani profile. However, these combinations yield density increases relative to peridotite (~3–5%) that violate neutral buoyancy constraints (see below). More reasonable fractions of eclogite (~20 vol.%) added to peridotite produce relatively minimal $V_s$ excesses that do not match the observed high velocities (Figure 9a), even for the fastest peridotite and eclogite compositions.

By contrast, the forward models that include peridotite + diamond mixtures suggest that ~1–3 vol.% diamond in peridotite can match the observed cratonic average $V_s$ profiles for $Q_0 = 35$–40 mW/m², with a negligible associated density increase (≤0.1%). More significant diamond fractions (~4–6 vol.%) are

required for the hottest geotherm ($Q_0$ = 45 mW/m$^2$). If 20 vol.% eclogite is included in the diamond + peridotite mixtures, the fraction of diamond required to achieve the cratonic average $V_s$ decreases slightly but is still ~1–3 vol.% for the two cooler geotherms (Figure 9c). Importantly, the addition of diamond is necessarily constrained to depths at which diamond is stable at the expense of graphite (Day, 2012), that is, >100 km depth for a 35 mW/m$^2$ geotherm, increasing to >180 km depth for a 45 mW/m$^2$ geotherm. This consideration is critical because the $G_s$ of graphite is an order of magnitude lower than diamond at ambient conditions (Blakslee et al., 1970; Gillis, 1984), and graphite has a significantly lower $V_s$ (~4.0 km/s: Figure 6) than diamond. Adding graphite to the mixing models introduces a stepwise, geotherm-dependent increase in calculated $V_s$; this is mostly due to higher diamond $V_s$ relative to peridotite, because the addition of small graphite volume fractions represents a negligible velocity decrease relative to bulk peridotite (Figure 9b) and the presence of ~20 vol.% eclogite entirely cancels out this decrease (Figure 9c). It is unlikely that the graphite-diamond transition is as sharp in nature as it is modeled in Figures 9b and 9c. For example, reactions between the two phases are kinetically inhibited, such that some experiments have produced coexisting diamond and graphite at relevant $P$-$T$ conditions (e.g., Sokol et al., 2001). The phase boundary itself is unlikely to have remained at a stable depth over geologic time, given evidence for fluctuating cratonic geotherms (e.g., Bell et al., 2003). Further, graphite or diamond shielded from the rock matrix as mineral inclusions at depth (e.g., in olivine or garnet) is relatively insensitive to changes in external $P$ and $T$ (Zhang, 1998). Alternatively, the diamond fraction may gradually increase with depth (e.g., the emplacement model of Smith et al., 2016). We therefore suggest that the modeled stepwise graphite-diamond transition along each geotherm is more likely to be expressed as a broad region of graphite-diamond coexistence, which would not result in a sharp $V_s$ increase observable by, e.g., receiver functions.

A final consideration is that of the lithosphere-asthenosphere boundary (LAB), which we define here as the depth at which the conductive geotherm intersects the 1350 °C mantle adiabat (Figures 7–9). For the coolest geotherm modeled in this study (35 mW/m$^2$), the LAB is >300 km, which is deeper than the LAB beneath Archean cratons inferred from seismic studies (e.g., Yuan & Romanowicz, 2010); for the hotter geotherms, the LAB decreases to ~230 km (40 mW/m$^2$) and ~170 km (45 mW/m$^2$). In the case of the 45 mW/m$^2$ geotherm, the diamond/graphite boundary is deeper than the LAB; this implies that if diamond is responsible for the observed high $V_s$, it would be present at significant concentrations in asthenospheric mantle rather than the lithosphere for the hottest cratons.

## 5. Buoyancy Constraints

An upper limit on the fraction of eclogite and diamond in the cratonic lithosphere arises from the absence of gravity anomalies beneath cratons (Eaton & Claire Perry, 2013; Kelly et al., 2003; Perry et al., 2003; Shapiro et al., 1999), consistent with the "isopycnic" hypothesis (Jordan, 1978) that depletion and melt extraction from the cratonic mantle lithosphere have yielded neutrally buoyant, stable cratonic roots. Other studies have shown that cratonic peridotite xenoliths can be either neutrally or positively buoyant at their calculated equilibration depths (James et al., 2004; Kelly et al., 2003; Lee, 2003; Poudjom Djomani et al., 2001). If the cratonic lithosphere is neutrally buoyant, we can establish the maximum fraction of eclogite that can be hosted by peridotite using density constraints.

Using the Perple_X-calculated densities of each peridotite and eclogite composition along each geotherm (Data Set S3), we calculated the density difference between each lithology and the asthenospheric mantle; for the latter, we assumed a pyrolite mantle composition (Workman & Hart, 2005) and used Perple_X to calculate the density along a 1623 K mantle adiabat (Figure 10a). Over the same depths as the observed high $V_s$, peridotite ranges from <5% negatively buoyant to <5% positively buoyant, whereas eclogite is negatively buoyant over the entire range; for both lithologies, buoyancy relative to asthenosphere increases with depth. The peridotite transition from negative to positive buoyancy is strongly compositional and temperature dependent, and ranges from ~3 to 6 GPa (similar to the results of Kelly et al., 2003). We also calculated mixtures of eclogite and peridotite such that the density difference between adiabatic mantle pyrolite and the cratonic peridotite-eclogite mixture at the same depth is zero (i.e., isopycnicity: Figure 10b). Using this approach, the maximum permitted vol.% eclogite increases with depth from zero to ~20 vol.% (35 mW/m$^2$), ~40 vol.% (40 mW/m$^2$), and ~60 vol.% (45 mW/m$^2$). However, these values assume isopycnicity between eclogite and peridotite at each specific depth interval; if deviations from neutral buoyancy are
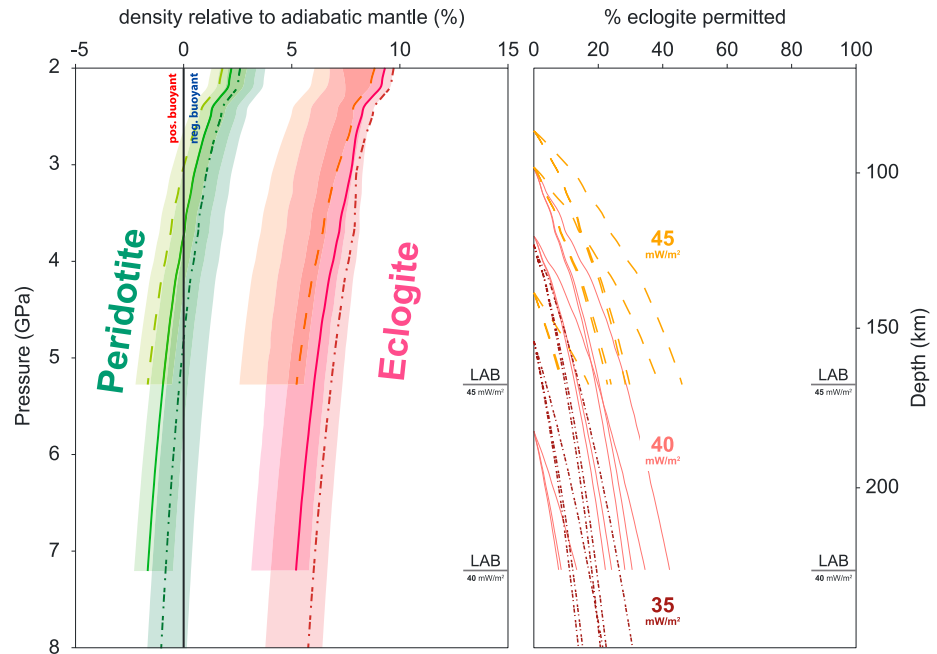
**Figure 10.** Summary of peridotite and eclogite constraints on lithospheric density/buoyancy. (a) Calculated peridotite or eclogite density along a cratonic geotherm relative to asthenosphere along an adiabat at the same depths, for the geotherms and 1623 K mantle adiabat in Figure 7 and the peridotite and eclogite compositions in Table S1. The lines and shading are as in Figure 9. (b) Maximum vol.% eclogite permitted at each depth in the case that eclogite + peridotite is neutrally buoyant relative to asthenosphere, calculated over regions in which peridotite alone is positively buoyant. Each color is for a distinct geotherm, and each line represents a mechanical mixture of either minimum, average, or maximum peridotite and eclogite composition (a total of nine mixtures per geotherm).

integrated over the entire lithosphere for each geotherm, we calculate that a maximum ~5–10 vol.% eclogite is permitted from 1 GPa to the LAB. Because we are interested in velocity anomalies that span ~50–75% of cratonic lithospheric thickness, we estimate a maximum permissible eclogite volume fraction of ~20% for our depth interval of interest.

Like eclogite, diamond is denser than peridotite in the depth range 100–200 km, but the small modal diamond fractions calculated in our models (~1–3 vol.%) yield a negligible density increase relative to peridotite alone. Further, calculated diamond densities from 2 to 8 GPa are equivalent to or lower than eclogite, in which case the maximum calculated eclogite fraction is also an upper bound on the diamond fraction.

## 6. Electrical Conductivity Constraints

Electrical conductivity provides an additional observable that can be tested against the mineralogical models. Variations in natural geomagnetic and geoelectric fields induce subsurface electric currents that can be probed by magnetotelluric sounding, where data can be either forward modeled or inverted to yield electrical conductivity profiles as a function of depth. These techniques have evolved in recent years to the extent that 2-D and 3-D models can be constructed, providing a more detailed picture of how electrical conductivity varies within cratons (Figure S12). Cratonic roots are generally more resistive than the surrounding mantle, although some more conductive regions have been identified. For example, high conductivities in the North American Slave and Superior Cratons have been attributed to metasomatism (Chen, Rondenay, et al., 2009). For this study, we compared conductivities under cratons at depths corresponding to the high shear-wave velocities ($V_s$, black outlined box in Figure S12), neglecting the higher conductivities thought to arise from secondary processes.

The electrical conductivity of a rock assemblage can be calculated based on the results of measurements carried out in the laboratory. We tested viable mineralogical combinations that can explain the fast cratonic $V_s$—presented in the previous section—by comparing their calculated electrical conductivities with existing electrical conductivity profiles for the cratonic lithosphere obtained from magnetotelluric studies. In order to

carry out the calculations, we assumed dry mineral assemblages (based on observations that cratonic lithosphere is dry at shallower than ~150 km depths: e.g., Hirth et al., 2000; Peslier et al., 2010). In contrast, hydrated conditions would increase electrical conductivity (Jones et al., 2012; Karato, 1990; Yoshino & Katsura, 2013) without affecting seismic velocities (Cline II et al., 2018).

For olivine, pyroxenes, and garnet, we employed conductivity laws from Jones et al. (2013) (mainly based on Fullea et al., 2011, for dry conditions) that account for the pressure and temperature dependence of conduction mechanisms, although only small polaron conduction (related to the iron content) is expected at the conditions of the cratonic lithosphere. In some of our mineralogical models, the calculated equilibrium eclogite mineral assemblage includes coesite (cf. Figure S9). Like diamond, coesite is a wide electronic band-gap insulator, and the electrical conductivity of both minerals is very low and relies on the presence of impurities in their structures. Further, there are no published coesite or diamond conductivity laws that account for the relevant *P-T* ranges. We therefore fixed the electrical conductivity of coesite to zero in our calculations, whereas for diamond we used an Arrhenius model based on conductivity measurements of natural type IIa diamonds at ambient pressure between 673 and 1523 K (Vandersande & Zoltan, 1991). At room temperature, the conductivity of high-purity type IIa diamonds is approximately 4 orders of magnitude lower than the conductivity of type I diamonds (Vandersande & Zoltan, 1991). Therefore, Type IIa diamond conductivity is a lower bound for natural diamonds in the cratonic lithosphere.

We estimated the electrical conductivities of the average peridotite and average eclogite compositions for both the cold and average geotherms ($Q_0 = 35$ mW/m$^2$ and 40 mW/m$^2$, respectively). We computed both self-consistent estimates (Bruggeman, 1935; Landauer, 1952) and bounds for the conductivities of peridotite and eclogite using a Hashin-Shtrikman (HS) averaging scheme (Berryman, 1995; Hashin & Shtrikman, 1962). The self-consistent estimate $\sigma_{SC}$ is obtained by iteratively solving:

$$\sum_{i=1}^{N} x_i \frac{\sigma_i - \sigma_{SC}}{\sigma_i + 2\sigma_{SC}} = 0$$

where $x_i$ and $\sigma_i$ are the volume fraction and electrical conductivity of component *i* and *N* is the number of mixture components. The HS lower ($\sigma_{HS^-}$) and upper ($\sigma_{HS^+}$) bounds are given by the following equations:

$$\sigma_{HS^-} = \left(\sum_{i=1}^{N} \frac{x_i}{\sigma_i + 2\min(\sigma)}\right)^{-1} - 2\min(\sigma)$$

$$\sigma_{HS^+} = \left(\sum_{i=1}^{N} \frac{x_i}{\sigma_i + 2\max(\sigma)}\right)^{-1} - 2\max(\sigma)$$

The self-consistent estimate can be considered as the electrical conductivity of an average host media composed of spherical inclusions of different components, whereas the HS bounds assume an isotropic polycrystal (Berryman, 1995). For this reason, we do not include graphite in our electrical conductivity models and limit them to the diamond stability field. Graphite has a very high electrical conductivity; if it formed an interconnected network, the electrical conductivity of the assemblage would equal that of graphite, and the employed averaging scheme would fail. However, recent experiments indicate that graphite forms isolated grains in peridotite and therefore does not enhance the bulk electrical conductivity (Zhang & Yoshino, 2017).

Figure 11a shows end-member peridotite, eclogite, and diamond electrical conductivity profiles; as expected, the end-member conductivity profiles depend strongly on the geotherm considered. Along the average geotherm ($Q_0 = 40$ mW/m$^2$), eclogite conductivity increases from $10^{-3}$ to ~$10^{-1}$ S/m between 4 and 8 GPa. Over the same pressure range, peridotite and diamond conductivities range between $2 \times 10^{-4}$– $2 \times 10^{-2}$ S/m and $10^{-6}$–$10^{-5}$ S/m, respectively. The difference between peridotite and eclogite conductivities results from (i) differences in iron content and (ii) the presence of garnet in the eclogite. For all eclogite, peridotite, and diamond, the cold geotherm ($Q_0 = 35$ mW/m$^2$) conductivities are at least 1 order of magnitude less than those along the average geotherm.

Finally, we calculated the bulk electrical conductivity for the mineralogical mixtures that satisfy the $V_s$ and density constraints (peridotite + 20% eclogite, peridotite + 2% diamond, and peridotite + 20%
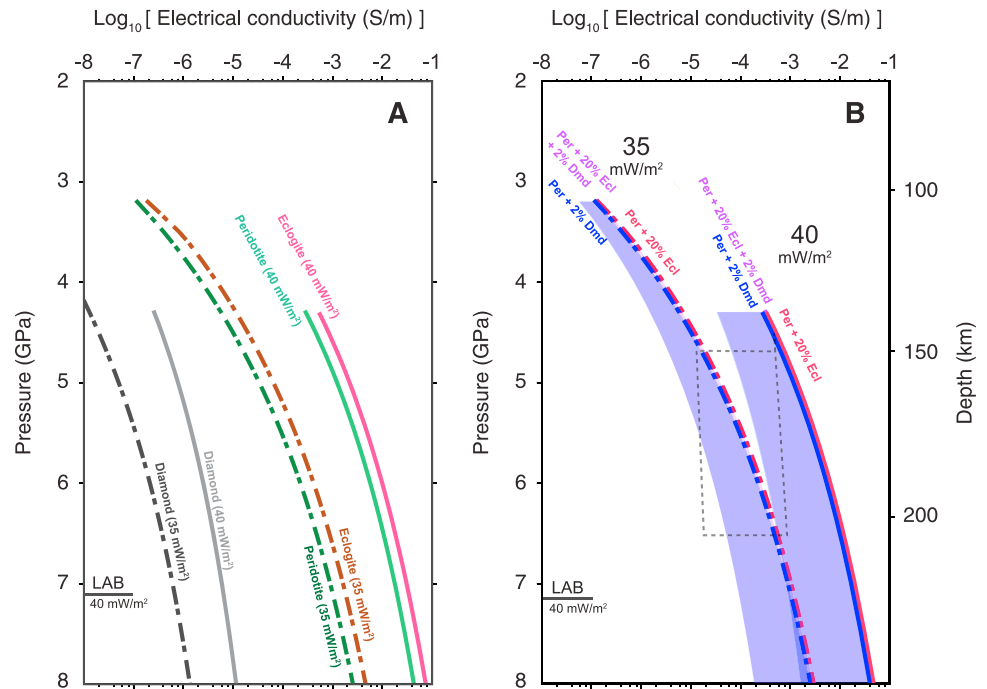
**Figure 11.** Electrical conductivities calculated from the mineralogical models and comparison with electrical conductivities derived from magnetotelluric regional measurements. (a) Self-consistent estimates of average cratonic peridotite, average cratonic eclogite, and diamond along the average (continuous lines) and cold (dash-dotted lines) cratonic geotherms corresponding to surface fluxes of 40 and 35 mW/m², respectively. (b) Peridotite + eclogite (red), peridotite + diamond (blue), and peridotite + 20 vol.% eclogite + diamond (purple) assemblages that match $V_s$ along the average (continuous lines) and cold (dash-dotted lines) cratonic geotherms. The colored areas delimit the Hashin-Shtrikman bounds corresponding the self-consistent estimate of the same color. The dashed grey line encloses the range of electrical conductivity derived from magnetotelluric measurements relevant to the high shear-wave velocity region (see black outlined box in Figure S12).

eclogite + 2% diamond). A further level of averaging was added to the calculation, in that we calculated conductivities with the volume fractions of each eclogite, peridotite, and diamond, and their respective self-consistent conductivity estimates. Figure 11b shows that all of the mineralogical combinations calculated in the previous section to bracket the observed $V_s$ are consistent with electrical conductivity profiles obtained from magnetotelluric measurements of the cratonic lithosphere in the depth range ~150–200 km where cratonic lithosphere is considered to be dry. All peridotite + 20% eclogite (red curves), peridotite + 2% diamond (blue curves), and peridotite + 20% eclogite + 2% diamond (purple curves) mixtures yield conductivities intermediate between end-member peridotite and eclogite. Even with a difference in electrical conductivity of 3 to 4 orders of magnitude between peridotite and diamond, 2 vol.% diamond has a negligible effect on the self-consistent estimates of bulk conductivity for peridotite + diamond mixtures compared to pure peridotite. The most notable effect of adding diamond is the decrease of the low-HS bound by one order of magnitude.

Hence, all of our mineralogical models are compatible with the results of the magnetotelluric measurements. Though the comparison of observed and calculated conductivities does not discriminate between mineralogical models, it provides the important confirmation that the mineralogical models involving eclogite and/or diamond are consistent with geophysical observations.

## 7. Discussion

Assuming eclogite and/or diamond are responsible for the high $V_s$ in cratonic roots (section 4.1 and Text S3), our mineralogical models suggest that ~1–3 vol.% diamond or ≫20 vol.% eclogite added to peridotite can independently satisfy the $V_s$ (Figure 9) and electrical conductivity (Figure 11) constraints along cold and

average cratonic geotherms. The neutral buoyancy constraint additionally suggests that eclogite abundances are unlikely to exceed ~20 vol.% throughout the lithosphere (Figure 10), requiring instead that peridotite + diamond or peridotite + eclogite + diamond mixtures be invoked to explain the $V_s$ results. Though the electrical conductivity data are compatible with multiple geotherms, the modeled $V_s$ and buoyancy results are highly dependent on the geotherm: cooler geotherms require less eclogite to keep the cratonic root neutrally buoyant, lower estimates of diamond to match the high $V_s$, a larger diamond stability field, and a deeper LAB (Figures 7–10). In this study (Figure 7) and others (Hasterok & Chapman, 2011; Rudnick et al., 1998), cratonic xenolith $P$-$T$ data converge on a global average $Q_0$ of ~40 mW/m$^2$ (i.e., an ~200-km-thick cratonic lithosphere), suggesting that the intermediate geotherm in our study is the most representative. Considering the $V_s$-matched mixing models alone, this result requires a *minimum* of ~2 vol.% diamond (Figures 9b and 9c). However, kimberlites hosting garnet peridotite xenoliths predominantly occur at the edges of cratons (Figure 2), such that the resulting average xenolith-derived geotherm may not represent temperatures in the seismically fastest portions in craton interiors. Some studies have further found that cratonic shear-wave velocities ($V_s$) can be matched with peridotite if the cratonic thermal structure is significantly cooler (100–200 K) at any given depth than determined from xenolith thermobarometry (e.g., Eeken et al., 2018). Though there is evidence for non–steady state thermal perturbations in some calculated xenolith $P$-$T$ conditions, it is typically assumed that at least some of the xenolith suite represents steady state conditions (e.g., Bell et al., 2003). It could also be argued that the xenolith-derived geotherms represent past temperatures in the lithospheric roots—which may be cooler at present—but peridotites and eclogite along geotherms significantly cooler than the coldest geotherm calculated in this study ($Q_0$~35 mW/m$^2$) may violate electrical conductivity constraints (e.g., Figure 11). Further, the lack of significant chemical zoning in the minerals of coarse-grained cratonic peridotites (e.g., Gurney et al., 1975) suggests equilibration at the time of eruption. Therefore, if the coolest calculated xenolith $P$-$T$ conditions reflect an average steady state conductive cratonic geotherm, even depleted peridotites with 20% eclogite cannot explain the cratonic average $V_s$; instead, the forward models suggest the presence of at least ~1 vol.% diamond.

Our results are also sensitive to composition: the modeled bulk craton $V_s$ increases with more depleted, MgO-rich peridotites and more Al$_2$O$_3$-rich, mid-ocean ridge basalt-like eclogites (Figures 8a and 8b). More depleted peridotites and more basaltic eclogites would therefore shift the required diamond abundances to slightly lower values, though they still lie between ~1 and 3 vol.% for the cold and average geotherms. Peridotite and eclogite composition also impacts buoyancy constraints because depleted, MgO-rich peridotites and eclogites are less dense than their fertile, MgO-poor counterparts. Considering the sum of our results, we suggest that a combination of ≤20 vol.% eclogite with ~2 vol.% diamond is the most consistent solution arising from all constraints described here. It has been suggested elsewhere that cratonic $V_s$ may be matched by highly depleted peridotites (e.g., harzburgites or dunites: Afonso et al., 2008; Eeken et al., 2018); though these bulk compositions yield faster $V_s$ than compositionally average cratonic peridotites, our calculations show that they do not achieve the seismically observed craton average $V_s$. Further, even if forward-modeled $V_s$ for such highly depleted peridotites were to match the craton average $V_s$, it would require that cratonic lithosphere was composed solely of the end-member, most-depleted lithologies, in contrast to the compositional diversity observed in cratonic xenolith suites (e.g., Griffin et al., 2002).

In comparing our results to studies of kimberlites and their xenoliths, we note that there are limited constraints on the abundance of eclogite and diamond in cratonic roots (section 3.1). Bulk garnet concentrates from kimberlites suggest a maximum volume fraction of ~2–10% eclogite in the cratonic mantle lithosphere, even for kimberlites in which the xenolith population is almost entirely eclogite (e.g., Griffin, Fisher, et al., 1999; McLean et al., 2007; Schulze, 1989). Bulk kimberlite diamond concentrations are typically <0.00002 vol.% (e.g., Bliss, 1992; Pearson et al., 2003) but individual diamond-bearing xenoliths—especially eclogites—may have >2 vol.% diamond (e.g., Anand et al., 2004; Viljoen et al., 2004, 1992). An association between diamonds and eclogite is further evident in the abundance of kimberlitic diamonds with eclogitic inclusion suites (~33%), which is higher than eclogite abundance in cratonic lithosphere (~2–20 vol.%: Schulze, 1989; this study). This may be due to diamond formation mechanisms in the lithosphere that are governed by redox interactions between rocks and C–O–H fluids and/or melts: the high redox buffering capacity of Fe-bearing eclogite makes it a particularly fortuitous diamond host (e.g., Luth & Stachel, 2014; Stachel & Luth, 2015). Other diamond formation mechanisms may be favored in harzburgites or dunites, for example, cooling and decreasing solubility of carbon in a reduced C–O–H fluid (e.g., Luth & Stachel, 2014). Because
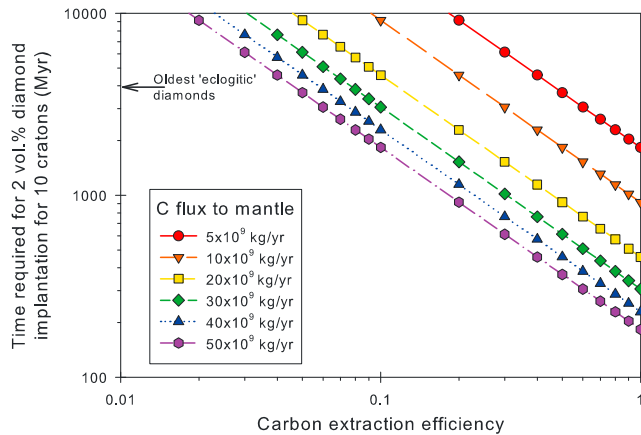
**Figure 12.** Timescales for 2 vol.% diamond implantation into 10 cratonic roots. Each curve represents a different potential mantle carbon flux to the lithosphere; varying the efficiency of carbon transfer from rising C–O–H fluids (x axis) changes the timescale required to implant our proposed diamond abundance (y axis).

there are numerous models for the presence of diamond and eclogite in cratonic lithosphere (e.g., Helmstaedt & Schulze, 1989; Palyanov et al., 2013; Shirey & Richardson, 2011; Walter et al., 2011; Weiss et al., 2015), further refinement of seismic models—not only for $V_s$ but also for $V_p$ and density—may help clarify the amount and distribution of eclogite and diamond in cratonic roots, and thus shed light on their origin. Still, the considerations discussed here suggest that the most reasonable solution to the high $V_s$ observation is not end-member eclogite or diamond, but more likely a genetically related and coupled suite of both: the reducing capacity of eclogite in the lithosphere may have produced higher diamond abundances that would not have been present with peridotite alone. Importantly, our proposed cratonic diamond fractions do not constrain the presence of carbon elsewhere in the cratonic lithosphere or in the rest of the mantle. It is possible that deep cratonic lithosphere (i.e., in the diamond stability field) is anomalously carbon-rich compared to shallow cratonic lithosphere due to underplating by subducted mid-ocean ridge basalt (Shirey & Richardson, 2011; Stachel & Harris, 2008), or transport from highly reducing deep mantle regions (e.g., Smith et al., 2016). On the other hand, it has been suggested that the mid-lithospheric discontinuity observed in some cratons may arise from a layer of carbonated phases or frozen-in melts (Eeken et al., 2018; Rader et al., 2015), in which case both shallow and deep cratonic lithosphere may be carbon-rich. Ultimately, given that the diamond fractions proposed here are a small fraction of total mantle carbon (see below), there must be other significant mantle carbon reservoirs, and our study has no implications for their setting or redox state.

Using the ~2 vol.% diamond case, we calculated the resulting amount of carbon that would be contained in cratonic roots. Assuming a cratonic root consisting of an inverted cone with a 1,000 km base and 50 km height, the mass of carbon (as diamond) in such a root would be ~$10^{18}$ kg today. If 10 such cratonic roots existed globally, the total mass of cratonic lithospheric mantle carbon would be ~$10^{19}$ kg, equivalent to 2.5 ppm C relative to bulk silicate Earth (BSE; assuming the BSE is two thirds the mass of the total Earth). This estimate constitutes ~2% of the BSE carbon (120 ppm: McDonough & Sun, 1995) and ~0.8–12.5% of the "modern" mantle reservoir (0.8–12.5 × $10^{20}$ kg C: Dasgupta & Hirschmann, 2010). Using this estimate for total lithosphere-hosted diamond (~$10^{19}$ kg C), and recognizing that rising C–O–H fluids may precipitate ~0.5–2 g C per 100 g fluid from ~200 to 120 km (Luth & Stachel, 2014), a total C–O–H fluid mass of 5 × $10^{20}$–2 × $10^{21}$ kg must have flowed through the cratonic lithosphere to implant this diamond. This fluid concentration is almost certainly an overestimate because it only accounts for diamond precipitation due to oversaturation in the fluid, whereas the redox capacity of eclogite could result in further carbon extraction from rising fluids than from cooling and decompression alone. Additionally, such fluid flux would likely be punctuated over Earth history, because diamond inclusion dates are not evenly distributed (e.g., Shirey & Richardson, 2011; Stachel & Luth, 2015).

Recognizing that diamonds form from both mantle carbon and subducted organic carbon (e.g., Cartigny et al., 2014; Ickert et al., 2013), we can further compare the amount of sequestered carbon to estimated modern subduction-related carbon fluxes into the deeper mantle beyond arcs, which are on the order of ~0.0001–52 Mt C/year ≈ 1 × $10^5$–52 × $10^9$ kg C/year (Dasgupta & Hirschmann, 2010; Kelemen & Manning, 2015). Figure 12 shows the potential timescales of diamond implantation into the cratonic roots given (i) our postulate for the total amount of carbon in cratonic lithosphere of 2 vol.% for 10 cratons (~$10^{19}$ kg C), (ii) a mantle carbon flux of 5–50 Mt C/year, and (iii) a range in efficiency of carbon extraction from the mantle to the lithosphere (1–100%), that is, how much of the deeply subducted C is transferred to the cratonic lithosphere. For the parameter space considered here, the time required to emplace 2 vol.% diamond in 10 cratonic roots is >180 Myr. We acknowledge that carbon ingassing via subduction in the early Earth was likely a less efficient process (e.g., Dasgupta & Hirschmann, 2010), therefore requiring longer timescales to reach 2 vol.% diamond in the cratonic roots. Additionally, the flux of mantle carbon (i.e., not subducted organic carbon) into cratonic lithosphere is unknown. Nevertheless, these calculations show that our proposed abundance of diamond in the lithospheric mantle represents a small fraction of the total terrestrial carbon budget and could have been transferred to cratonic roots over reasonable geologic timescales.

## 8. Conclusions

1. Many global- and continental-scale seismic tomography models exhibit a $V_s$ excess in the deep cratonic lithosphere relative to $V_s$ of cratonic peridotites alone. Synthetic seismograms obtained in these fast-$V_s$ models (using 3-D numerical wavefield computations) provide significantly better fits to the observed seismic waveforms than slower-$V_s$ models that are compatible with peridotitic compositions.

2. Using cratonic geotherms that fit cratonic xenolith *P-T* data, mineralogical and petrological mixing models can reproduce the observed $V_s$ with 1–3 vol.% diamond or ≫20 vol.% eclogite. These results are inversely related; more eclogite implies less diamond. Other minerals or chemical components may modulate these results but are less likely than eclogite and/or diamond, as they would have to be present in greater abundances to account for their lower $V_s$ relative to diamond.

3. Buoyancy constraints and the absence of a gravity anomaly suggests that no more than ~20 vol.% eclogite is present in the cratonic lithosphere.

4. Electrical conductivity constraints are compatible with all of the mixing model results. Though diamond is significantly less conductive than either peridotite or eclogite, even 6 vol.% diamond added to either lithology is still compatible with observations.

5. Using the most representative cratonic geotherms (35–40 mW/m$^2$) and considering all constraints, our best estimates for the permissible volume fractions of eclogite and diamond in the cratonic lithosphere are ≤20 and ~2 vol.%, respectively.

6. Our estimate for the fraction of eclogite in cratonic lithosphere is higher than (but not significantly different from) estimates derived from kimberlite garnet concentrate chemistry. Likewise, the proposed ~1–3 vol.% diamond is consistent with (i) diamond concentrations in individual xenoliths, especially eclogite; (ii) estimates of total carbon in the BSE and mantle; and (iii) geologically reasonable timescales over which this carbon could have been implanted in cratonic roots.

## References

Abers, G. A., & Hacker, B. R. (2016). A MATLAB toolbox and Excel workbook for calculating the densities, seismic wave speeds, and major element composition of minerals and rocks at pressure and temperature. *Geochemistry, Geophysics, Geosystems*, *17*, 616–624. https://doi.org/10.1002/2015GC006171

Afonso, J. C., Fernàndez, M., Ranalli, G., Griffin, W. L., & Connolly, J. A. D. (2008). Integrated geophysical-petrological modeling of the lithosphere and sublithospheric upper mantle: Methodology and applications. *Geochemistry, Geophysics, Geosystems*, *9*, Q05008. https://doi.org/10.1029/2007GC001834

Anand, M., Taylor, L. A., Misra, K. C., Carlson, W. D., & Sobolev, N. V. (2004). Nature of diamonds in Yakutian eclogites: Views from eclogite tomography and mineral inclusions in diamonds. *Lithos*, *77*(1–4), 333–348. https://doi.org/10.1016/j.lithos.2004.03.026

Aoki, K. I., & Kushiro, I. (1968). Some clinopyroxenes from ultramafic inclusions in Dreiser Weiher, Eifel. *Contributions to Mineralogy and Petrology*, *18*(4), 326–337. https://doi.org/10.1007/BF00399694

Auer, L., Boschi, L., Becker, T. W., Nissen-Meyer, T., & Giardini, D. (2014). Savani: A variable resolution whole-mantle model of anisotropic shear velocity variations based on multiple data sets. *Journal of Geophysical Research: Solid Earth*, *119*, 3006–3034. https://doi.org/10.1002/2013JB010773

Aulbach, S., & Jacob, D. E. (2016). Major- and trace-elements in cratonic mantle eclogites and pyroxenites reveal heterogeneous sources and metamorphic processing of low-pressure protoliths. *Lithos*, *262*, 586–605. https://doi.org/10.1016/j.lithos.2016.07.026

Babuška, V., Montagner, J. P., Plomerová, J., & Girardin, N. (1998). Age-dependent large-scale fabric of the mantle lithosphere as derived from surface-wave velocity anisotropy. *Pure and Applied Geophysics*, *151*(4), 257–280. https://doi.org/10.1007/s000240050114

Bao, X., Dalton, C. A., Jin, G., Gaherty, J. B., & Shen, Y. (2016). Imaging Rayleigh wave attenuation with USArray. *Geophysical Journal International*, *206*(1), 241–259. https://doi.org/10.1093/gji/ggw151

Bass, J. D. (1986). Elasticity of uvarovite and andradite garnets. *Journal of Geophysical Research*, *91*(B7), 7505–7516. https://doi.org/10.1029/JB091iB07p07505

Bell, D. R., Schmitz, M. D., & Janney, P. E. (2003). Mesozoic thermal evolution of the southern African mantle lithosphere. *Lithos*, *71*(2), 273–287. https://doi.org/10.1016/S0024-4937(03)00117-8

Berryman, J. G. (1995). *Mixture theories for rock properties* (pp. 205–228). Washington, DC: American Geophysical Union.

Blakslee, O. L., Proctor, D. G., Seldin, E. J., Spence, G. B., & Weng, T. (1970). Elastic constants of compression-annealed pyrolytic graphite. *Journal of Applied Physics*, *41*(8), 3373–3382. https://doi.org/10.1063/1.1659428

Bliss, J. D. (1992). Grade-tonnage and other models for diamond kimberlite pipes. *Nonrenewable Resources*, *1*(3), 214–230. https://doi.org/10.1007/BF01782275

Bodin, T., Leiva, J., Romanowicz, B., Maupin, V., & Yuan, H. (2016). Imaging anisotropic layering with Bayesian inversion of multiple data types. *Geophysical Journal International*, *206*(1), 605–629. https://doi.org/10.1093/gji/ggw124

Boyd, F. R. (1973). A pyroxene geotherm. *Geochimica et Cosmochimica Acta*, *37*(12), 2533–2546. https://doi.org/10.1016/0016-7037(73)90263-9

Boyd, F. R. (1989). Compositional distinction between oceanic and cratonic lithosphere. *Earth and Planetary Science Letters*, *96*(1), 15–26. https://doi.org/10.1016/0012-821X(89)90120-9

Boyd, F. R., & Finnerty, A. A. (1980). Conditions of origin of natural diamonds of peridotite affinity. *Journal of Geophysical Research*, *85*(B12), 6911–6911. https://doi.org/10.1029/JB085iB12p06911

Boyd, F. R., & Gurney, J. J. (1986). Diamonds and the African lithosphere. *Science*, *232*(4749), 472–477. https://doi.org/10.1126/science.232.4749.472

Boyd, F. R., Pearson, D. G., Nixon, P. H., & Mertzman, S. A. (1993). Low-calcium garnet harzburgites from southern Africa: Their relations to craton structure and diamond crystallization. *Contributions to Mineralogy and Petrology*, *113*(3), 352–366. https://doi.org/10.1007/BF00286927

Bruggeman, D. A. G. (1935). Berechnung verschiedener physikalischer Konstanten von heterogenen Substanzen. *Annalen der Physik*, *416*(8), 665–679. https://doi.org/10.1002/andp.19354160802

Bruneton, M., Pedersen, H. A., Vacher, P., Kukkonen, I. T., Arndt, N. T., Funke, S., et al. (2004). Layered lithospheric mantle in the central Baltic Shield from surface waves and xenolith analysis. *Earth and Planetary Science Letters*, *226*(1), 41–52. https://doi.org/10.1016/j.epsl.2004.07.034

Calò, M., Bodin, T., & Romanowicz, B. (2016). Layered structure in the upper mantle across North America from joint inversion of long and short period seismic data. *Earth and Planetary Science Letters*, *449*(Supplement C), 164–175. https://doi.org/10.1016/j.epsl.2016.05.054

Canil, D., O'Neill, H. S. C., Pearson, D. G., Rudnick, R. L., McDonough, W. F., & Carswell, D. A. (1994). Ferric iron in peridotites and mantle oxidation states. *Earth and Planetary Science Letters*, *123*(1), 205–220. https://doi.org/10.1016/0012-821X(94)90268-2

Carlson, R. W., Pearson, D. G., & James, D. E. (2005). Physical, chemical, and chronological characteristics of continental mantle. *Reviews of Geophysics*, *43*, RG1001. https://doi.org/10.1029/2004RG000156

Cartigny, P., Palot, M., Thomassot, E., & Harris, J. W. (2014). Diamond formation: A stable isotope perspective. *Annual Review of Earth and Planetary Sciences*, *42*(1), 699–732. https://doi.org/10.1146/annurev-earth-042711-105259

Chang, S.-J., Ferreira, A. M. G., Ritsema, J., van Heijst, H. J., & Woodhouse, J. H. (2015). Joint inversion for global isotropic and radially anisotropic mantle structure including crustal thickness perturbations. *Journal of Geophysical Research: Solid Earth*, *120*, 4278–4300. https://doi.org/10.1002/2014JB011824

Chapman, D. S. (1986). Thermal gradients in the continental crust. *Geological Society, London, Special Publications*, *24*(1), 63–70. https://doi.org/10.1144/gsl.sp.1986.024.01.07

Chen, C.-W., Rondenay, S., Evans, R. L., & Snyder, D. B. (2009). Geophysical detection of relict metasomatism from an Archean (~3.5 Ga) subduction zone. *Science*, *326*(5956), 1089–1091. https://doi.org/10.1126/science.1178477

Chen, L., Cheng, C., & Wei, Z. (2009). Seismic evidence for significant lateral variations in lithospheric thickness beneath the central and western North China Craton. *Earth and Planetary Science Letters*, *286*(1), 171–183. https://doi.org/10.1016/j.epsl.2009.06.022

Chesley, J. T., Rudnick, R. L., & Lee, C.-T. (1999). Re-Os systematics of mantle xenoliths from the East African Rift: age, structure, and history of the Tanzanian craton. *Geochimica et Cosmochimica Acta*, *63*(7), 1203–1217. https://doi.org/10.1016/S0016-7037(99)00004-6

Cline, C. J. II, Faul, U. H., David, E. C., Berry, A. J., & Jackson, I. (2018). Redox-influenced seismic properties of upper-mantle olivine. *Nature*, *555*(7696), 355–358. https://doi.org/10.1038/nature25764

Clouzet, P., Masson, Y., & Romanowicz, B. (2018). Box Tomography: First application to the imaging of upper-mantle shear velocity and radial anisotropy structure beneath the North American continent. *Geophysical Journal International*, *213*(3), 1849–1875. https://doi.org/10.1093/gji/ggy078

Connolly, J. A. D. (2009). The geodynamic equation of state: What and how. *Geochemistry, Geophysics, Geosystems*, *10*, Q10014. https://doi.org/10.1029/2009GC002540

Connolly, J. A. D., & Kerrick, D. M. (2002). Metamorphic controls on seismic velocity of subducted oceanic crust at 100–250 km depth. *Earth and Planetary Science Letters*, *204*(1), 61–74. https://doi.org/10.1016/S0012-821X(02)00957-3

Creighton, S., Stachel, T., Eichenberg, D., & Luth, R. W. (2010). Oxidation state of the lithospheric mantle beneath Diavik diamond mine, central Slave craton, NWT, Canada. *Contributions to Mineralogy and Petrology*, *159*(5), 645–657. https://doi.org/10.1007/s00410-009-0446-x

Creighton, S., Stachel, T., Matveev, S., Höfer, H., McCammon, C., & Luth, R. W. (2009). Oxidation of the Kaapvaal lithospheric mantle driven by metasomatism. *Contributions to Mineralogy and Petrology*, *157*(4), 491–504. https://doi.org/10.1007/s00410-008-0348-3

Cupillard, P., Delavaud, E., Burgos, G. l., Festa, G., Vilotte, J.-P., Capdeville, Y., & Montagner, J.-P. (2012). RegSEM: A versatile code based on the spectral element method to compute seismic wave propagation at the regional scale. *Geophysical Journal International*, *188*(3), 1203–1220. https://doi.org/10.1111/j.1365-246X.2011.05311.x

Dalton, C. A., Bao, X., & Ma, Z. (2017). The thermal structure of cratonic lithosphere from global Rayleigh wave attenuation. *Earth and Planetary Science Letters*, *457*, 250–262. https://doi.org/10.1016/j.epsl.2016.10.014

Danchin, R. V. (1979). *Mineral and bulk chemistry of garnet lherzolite and garnet harzburgite xenoliths from the Premier Mine, South Africa* (pp. 104–126). Washington, DC: American Geophysical Union.

Darbyshire, F. A., & Eaton, D. W. (2010). The lithospheric root beneath Hudson Bay, Canada from Rayleigh wave dispersion: No clear seismological distinction between Archean and Proterozoic mantle. *Lithos*, *120*(1), 144–159. https://doi.org/10.1016/j.lithos.2010.04.010

Darbyshire, F. A., Eaton, D. W., & Bastow, I. D. (2013). Seismic imaging of the lithosphere beneath Hudson Bay: Episodic growth of the Laurentian mantle keel. *Earth and Planetary Science Letters*, *373*, 179–193. https://doi.org/10.1016/j.epsl.2013.05.002

Dasgupta, R., & Hirschmann, M. M. (2010). The deep carbon cycle and melting in Earth's interior. *Earth and Planetary Science Letters*, *298*(1–2), 1–13. https://doi.org/10.1016/j.epsl.2010.06.039

Davies, G. R., Nixon, P. H., Pearson, D. G., & Obata, M. (1993). Tectonic implications of graphitized diamonds from the Ronda peridotite massif, southern Spain. *Geology*, *21*(5), 471–474. https://doi.org/10.1130/0091-7613(1993)021<0471:TIOGDF>2.3.CO;2

Day, H. W. (2012). A revised diamond-graphite transition curve. American Mineralogist, 97(1), GEOROC Database. Max Planck Institute for Chemistr-GEOROC Database. *Max Planck Institute for Chemistry*, *97*(1), 52–62. https://doi.org/10.2138/am.2011.3763

Debayle, E., Dubuffet, F., & Durand, S. (2016). An automatically updated *S*-wave model of the upper mantle and the depth extent of azimuthal anisotropy. *Geophysical Research Letters*, *43*, 674–682. https://doi.org/10.1002/2015GL067329

Dziewonski, A. M., & Anderson, D. L. (1981). Preliminary reference Earth model. *Physics of the Earth and Planetary Interiors*, *25*(4), 297–356. https://doi.org/10.1016/0031-9201(81)90046-7

Eaton, D. W., & Claire Perry, H. K. (2013). Ephemeral isopycnicity of cratonic mantle keels. *Nature Geoscience*, *6*(11), 967–970. https://doi.org/10.1038/ngeo1950

Eeken, T., Goes, S., Pedersen, H. A., Arndt, N. T., & Bouilhol, P. (2018). Seismic evidence for depth-dependent metasomatism in cratons. *Earth and Planetary Science Letters*, *491*, 148–159. https://doi.org/10.1016/j.epsl.2018.03.018

Ehrenberg, S. N., & Griffin, W. L. (1979). Garnet granulite and associated xenoliths in minette and serpentinite diatremes of the Colorado Plateau. *Geology*, *7*(10), 483–483. https://doi.org/10.1130/0091-7613

Faul, U., & Jackson, I. (2005). The seismological signature of temperature and grain size variations in the upper mantle. *Earth and Planetary Science Letters*, *234*(1), 119–134. https://doi.org/10.1016/j.epsl.2005.02.008

Faul, U., & Jackson, I. (2015). Transient creep and strain energy dissipation: An experimental perspective. *Annual Review of Earth and Planetary Sciences*, *43*(1), 541–569. https://doi.org/10.1146/annurev-earth-060313-054732

Faure, S. (2010). World kimberlites CONSOREM database (version 3). Consortium de Recherche en Exploration Minérale CONSOREM, Université du Québec à Montréal.

Ferreira, A. M. G., Woodhouse, J. H., Visser, K., & Trampert, J. (2010). On the robustness of global radially anisotropic surface wave tomography. *Journal of Geophysical Research: Solid Earth*, *115*, B04313. https://doi.org/10.1029/2009JB006716

Fichtner, A., Kennett, B. L. N., Igel, H., & Bunge, H.-P. (2010). Full waveform tomography for radially anisotropic structure: New insights into present and past states of the Australasian upper mantle. *Earth and Planetary Science Letters*, *200*, 270–280. https://doi.org/10.1016/j.epsl.2009.12.003

French, S. W., & Romanowicz, B. A. (2014). Whole-mantle radially anisotropic shear velocity structure from spectral-element waveform tomography. *Geophysical Journal International*, *199*(3), 1303–1327. https://doi.org/10.1093/gji/ggu334

Frost, D. J., & McCammon, C. A. (2008). The redox state of Earth's mantle. *Annual Review of Earth and Planetary Sciences*, *36*(1), 389–420. https://doi.org/10.1146/annurev.earth.36.031207.124322

Fullea, J., Muller, M. R., & Jones, A. G. (2011). Electrical conductivity of continental lithospheric mantle from integrated geophysical and petrological modeling: Application to the Kaapvaal Craton and Rehoboth Terrane, southern Africa. *Journal of Geophysical Research*, *116*, B10202. https://doi.org/10.1029/2011JB008544

Gibson, S. A., McMahon, S. C., Day, J. A., & Dawson, J. B. (2013). Highly refractory lithospheric mantle beneath the Tanzanian Craton: Evidence from Lashaine pre-metasomatic garnet-bearing peridotites. *Journal of Petrology*, *54*(8), 1503–1546. https://doi.org/10.1093/petrology/egt020

Gillis, P. P. (1984). Calculating the elastic constants of graphite. *Carbon*, *22*(4), 387–391. https://doi.org/10.1016/0008-6223(84)90010-1

Griffin, W. L., Doyle, B. J., Ryan, C. G., Pearson, N. J., Suzanne, Y. O., Davies, R., et al. (1999). Layered mantle lithosphere in the Lac de Gras Area, Slave Craton: Composition, structure and origin. *Journal of Petrology*, *40*(5), 705–727. https://doi.org/10.1093/petroj/40.5.705

Griffin, W. L., Fisher, N. I., Friedman, J., Ryan, C. G., & O'Reilly, S. Y. (1999). Cr-Pyrope garnets in the lithospheric mantle. I. Compositional systematics and relations to tectonic setting. *Journal of Petrology*, *40*(5), 679–704. https://doi.org/10.1093/petroj/40.5.679

Griffin, W. L., Fisher, N. I., Friedman, J. H., O'Reilly, S. Y., & Ryan, C. G. (2002). Cr-pyrope garnets in the lithospheric mantle 2. Compositional populations and their distribution in time and space. *Geochemistry, Geophysics, Geosystems*, *3*(12), 1073. https://doi.org/10.1029/2002GC000298

Griffin, W. L., O'Reilly, S. Y., Abe, N., Aulbach, S., Davies, R. M., Pearson, N. J., et al. (2003). The origin and evolution of Archean lithospheric mantle. *Precambrian Research*, *127*(1–3), 19–41. https://doi.org/10.1016/S0301-9268(03)00180-3

Gung, Y., Panning, M., & Romanowicz, B. (2003). Global anisotropy and the thickness of continents. *Nature*, *422*, 707. https://doi.org/10.1038/nature01559

Gurney, J. J., Harte, B., & Cox, K. G. (1975). 35—Mantle xenoliths in the matsoku kimberlite pipe. In L. H. Ahrens, J. B. Dawson, A. R. Duncan, & A. J. Erlank (Eds.), *Physics and Chemistry of the Earth* (pp. 507–523). Oxford: Pergamon Press.

Hacker, B. R., & Abers, G. A. (2004). Subduction factory 3: An Excel worksheet and macro for calculating the densities, seismic wave speeds, and $H_2O$ contents of minerals and rocks at pressure and temperature. *Geochemistry, Geophysics, Geosystems*, *5*, Q01005. https://doi.org/10.1029/2003GC000614

Hacker, B. R., Abers, G. A., & Peacock, S. M. (2003). Subduction factory 1. Theoretical mineralogy, densities, seismic wave speeds, and $H_2O$ contents. *Journal of Geophysical Research*, *108*(B1), 2029. https://doi.org/10.1029/2001JB001127

Hashin, Z., & Shtrikman, S. (1962). A variational approach to the theory of the effective magnetic permeability of multiphase materials. *Journal of Applied Physics*, *33*(10), 3125–3131. https://doi.org/10.1063/1.1728579

Hasterok, D., & Chapman, D. S. (2011). Heat production and geotherms for the continental lithosphere. *Earth and Planetary Science Letters*, *307*(1–2), 59–70. https://doi.org/10.1016/j.epsl.2011.04.034

Helmstaedt, H., & Schulze, D. J. (1989). Southern African kimberlites and their mantle sample: Implications for Archean tectonics and lithosphere evolution. *Kimberlites and Related Rocks*, *1*, 358–368.

Hieronymus, C. F., & Goes, S. (2010). Complex cratonic seismic structure from thermal models of the lithosphere: Effects of variations in deep radiogenic heating. *Geophysical Journal International*, *180*(3), 999–1012. https://doi.org/10.1111/j.1365-246X.2009.04478.x

Hills, D. V., & Haggerty, S. E. (1989). Petrochemistry of eclogites from the Koidu Kimberlite Complex, Sierra Leone. *Contributions to Mineralogy and Petrology*, *103*(4), 397–422. https://doi.org/10.1007/BF01041749

Hirsch, A. C., Dalton, C. A., & Ritsema, J. (2015). Constraints on shear velocity in the cratonic upper mantle from Rayleigh wave phase velocity. *Geochemistry, Geophysics, Geosystems*, *16*, 3982–4005. https://doi.org/10.1002/2015GC006066

Hirth, G., Evans, R. L., & Chave, A. D. (2000). Comparison of continental and oceanic mantle electrical conductivity: Is the Archean lithosphere dry? *Geochemistry, Geophysics, Geosystems*, *1*(12), 1030. https://doi.org/10.1029/2000GC000048

Holland, T. J. B., & Powell, R. (1998). An internally consistent thermodynamic data set for phases of petrological interest. *Journal of Metamorphic Geology*, *16*(3), 309–343. https://doi.org/10.1111/j.1525-1314.1998.00140.x

Hunt, L., Stachel, T., Grutter, H., Armstrong, J., McCandless, T. E., Simonetti, A., & Tappe, S. (2012). Small mantle fragments from the Renard kimberlites, Quebec: Powerful recorders of mantle lithosphere formation and modification beneath the Eastern Superior Craton. *Journal of Petrology*, *53*(8), 1597–1635. https://doi.org/10.1093/petrology/egs027

Ickert, R. B., Stachel, T., Stern, R. A., & Harris, J. W. (2013). Diamond from recycled crustal carbon documented by coupled $\delta^{18}O$–$\delta^{13}C$ measurements of diamonds and theirinclusions. *Earth and Planetary Science Letters*, *364*, 85–97. https://doi.org/10.1016/j.epsl.2013.01.008

Ionov, D. A., Doucet, L. S., & Ashchepkov, I. V. (2010). Composition of the lithospheric mantle in the Siberian Craton: New constraints from fresh peridotites in the Udachnaya-East kimberlite. *Journal of Petrology*, *51*(11), 2177–2210. https://doi.org/10.1093/petrology/egq053

Isaak, D. G., & Ohno, I. (2003). Elastic constants of chrome-diopside: Application of resonant ultrasound spectroscopy to monoclinic single-crystals. *Physics and Chemistry of Minerals*, *30*(7), 430–439. https://doi.org/10.1007/s00269-003-0334-2

Jackson, I., & Faul, U. (2010). Grainsize-sensitive viscoelastic relaxation in olivine: Towards a robust laboratory-based model for seismological application. *Physics of the Earth and Planetary Interiors*, *183*(1-2), 151–163. https://doi.org/10.1016/j.pepi.2010.09.005

Jacob, D. E., & Foley, S. F. (1999). Evidence for Archean ocean crust with low high field strength element signature from diamondiferous eclogite xenoliths. *Lithos*, *48*(1–4), 317–336. https://doi.org/10.1016/S0024-4937(99)00034-1

Jacob, D. E., Schmickler, B., & Schulze, D. J. (2003). Trace element geochemistry of coesite-bearing eclogites from the Roberts Victor kimberlite, Kaapvaal craton. *Lithos*, *71*(2–4), 337–351. https://doi.org/10.1016/S0024-4937(03)00120-8

Jacob, D. E., Viljoen, K. S., & Grassineau, N. V. (2009). Eclogite xenoliths from Kimberley, South Africa—A case study of mantle metasomatism in eclogites. *Lithos*, *112*, 1002–1013. https://doi.org/10.1016/j.lithos.2009.03.034

James, D. E., Boyd, F. R., Schutt, D., Bell, D. R., & Carlson, R. W. (2004). Xenolith constraints on seismic velocities in the upper mantle beneath southern Africa. *Geochemistry, Geophysics, Geosystems*, *5*, Q01002. https://doi.org/10.1029/2003GC000551

Jaques, A. L., O'Neill, H. S. C., Smith, C. B., Moon, J., & Chappell, B. W. (1990). Diamondiferous peridotite xenoliths from the Argyle (AK1) lamproite pipe, Western Australia. *Contributions to Mineralogy and Petrology*, *104*(3), 255–276. https://doi.org/10.1007/BF00321484

Jaupart, C., & Mareschal, J. C. (1999). The thermal structure and thickness of continental roots. *Lithos*, *48*(1–4), 93–114. https://doi.org/10.1016/S0024-4937(99)00023-7

Jones, A. G., Afonso, J. C., & Fullea, J. (2017). Geochemical and geophysical constrains on the dynamic topography of the Southern African Plateau. *Geochemistry, Geophysics, Geosystems*, *18*, 3556–3575. https://doi.org/10.1002/2017GC006908

Jones, A. G., Fishwick, S., Evans, R. L., Muller, M. R., & Fullea, J. (2013). Velocity-conductivity relations for cratonic lithosphere and their application: Example of Southern Africa. *Geochemistry, Geophysics, Geosystems*, *14*, 806–827. https://doi.org/10.1002/ggge.20075

Jones, A. G., Fullea, J., Evans, R. L., & Muller, M. R. (2012). Water in cratonic lithosphere: Calibrating laboratory-determined models of electrical conductivity of mantle minerals using geophysical and petrological observations. *Geochemistry, Geophysics, Geosystems*, *13*, Q06010. https://doi.org/10.1029/2012GC004055

Jordan, T. H. (1975). The continental tectosphere. *Reviews of Geophysics and Space Physics*, *13*, 1–12.

Jordan, T. H. (1978). Composition and development of the continental tectosphere. *Nature*, *274*(5671), 544–548. https://doi.org/10.1038/274544a0

Karato, S. (1990). The role of hydrogen in the electrical conductivity of the upper mantle. *Nature*, *347*(6290), 272–273. https://doi.org/10.1038/347272a0

Katayama, I., & Korenaga, J. (2011). Is the African cratonic lithosphere wet or dry? *Geological Society of America Special Papers*, *478*, 249–256. https://doi.org/10.1130/2011.2478(13)

Kelemen, P. B., & Manning, C. E. (2015). Reevaluating carbon fluxes in subduction zones, what goes down, mostly comes up. *Proceedings of the National Academy of Sciences of the United States of America*, *112*(30), E3997–E4006. https://doi.org/10.1073/pnas.1507889112

Kelly, R. K., Kelemen, P. B., & Jull, M. (2003). Buoyancy of the continental upper mantle. *Geochemistry, Geophysics, Geosystems*, *4*(2), 1017. https://doi.org/10.1029/2002GC000399

Kennett, B. L. N., Fichtner, A., Fishwick, S., & Yoshizawa, K. (2013). Australian Seismological Reference Model (AuSREM): mantle component. *Geophysical Journal International*, *192*(2), 871–887. https://doi.org/10.1093/gji/ggs065

Klemme, S., Ivanic, T. J., Connolly, J. A. D., & Harte, B. (2009). Thermodynamic modelling of Cr-bearing garnets with implications for diamond inclusions and peridotite xenoliths. *Lithos*, *112*, 986–991. https://doi.org/10.1016/j.lithos.2009.05.007

Komatitsch, D., & Tromp, J. (1999). Introduction to the spectral element method for three-dimensional seismic wave propagation. *Geophysical Journal International*, *139*(3), 806–822. https://doi.org/10.1046/j.1365-246x.1999.00967.x

Komatitsch, D., & Vilotte, J.-P. (1998). The spectral element method: An efficient tool to simulate the seismic response of 2D and 3D geological structures. *Bulletin of the Seismological Society of America*, *88*(2), 368–392.

Koornneef, J. M., Davies, G. R., Döpp, S. P., Vukmanovic, Z., Nikogosian, I. K., & Mason, P. R. D. (2009). Nature and timing of multiple metasomatic events in the sub-cratonic lithosphere beneath Labait, Tanzania. *Lithos*, *112*, 896–912. https://doi.org/10.1016/j.lithos.2009.04.039

Kopylova, M. G., Russell, J. K., & Cookenboo, H. (1999). Petrology of peridotite and pyroxenite xenoliths from the Jericho kimberlite: Implications for the thermal state of the mantle beneath the Slave Craton, Northern Canada. *Journal of Petrology*, *40*(1), 79–104. https://doi.org/10.1093/petroj/40.1.79

Landauer, R. (1952). The electrical resistance of binary metallic mixtures. *Journal of Applied Physics*, *23*(7), 779–784. https://doi.org/10.1063/1.1702301

Lazarov, M., Woodland, A. B., & Brey, G. P. (2009). Thermal state and redox conditions of the Kaapvaal mantle: A study of xenoliths from the Finsch mine, South Africa. *Lithos*, *112*, 913–923. https://doi.org/10.1016/j.lithos.2009.03.035

Lebedev, S., Boonen, J., & Trampert, J. (2009). Seismic structure of Precambrian lithosphere: New constraints from broad-band surface-wave dispersion. *Lithos*, *109*(1), 96–111. https://doi.org/10.1016/j.lithos.2008.06.010

Lee, C.-T. A. (2003). Compositional variation of density and seismic velocities in natural peridotites at STP conditions: Implications for seismic imaging of compositional heterogeneities in the upper mantle. *Journal of Geophysical Research*, *108*(B9), 2441. https://doi.org/10.1029/2003JB002413

Lee, C.-T. A., Luffi, P., & Chin, E. J. (2011). Building and destroying continental mantle. *Annual Review of Earth and Planetary Sciences*, *39*(1), 59–90. https://doi.org/10.1146/annurev-earth-040610-133505

Lee, C.-T. A., & Rudnick, R. L. (1997). Compositionally stratified cratonic lithosphere: Petrology and geochemistry of peridotite xenoliths from the Labait tuff cone, Tanzania. In J. J. Gurney, & S. R. Richardson (Eds.), *Proceedings of the 7th International Kimberlite Conference* (pp. 503–521). Cape Town: Red Roof Designs.

Lehnert, K., Su, Y., Langmuir, C. H., Sarbas, B., & Nohl, U. (2000). A global geochemical database structure for rocks. *Geochemistry, Geophysics, Geosystems*, *1*(5), 1–14. https://doi.org/10.1029/1999GC000026

Lekić, V., Panning, M., & Romanowicz, B. (2010). A simple method for improving crustal corrections in waveform tomography. *Geophysical Journal International*, *182*(1), 265–278. https://doi.org/10.1111/j.1365-246X.2010.04602.x

Lekic, V., & Romanowicz, B. (2011). Tectonic regionalization without a priori information: A cluster analysis of upper mantle tomography. *Earth and Planetary Science Letters*, *308*(1–2), 151–160. https://doi.org/10.1016/j.epsl.2011.05.050

Luth, R. W., & Stachel, T. (2014). The buffering capacity of lithospheric mantle: Implications for diamond formation. *Contributions to Mineralogy and Petrology*, *168*(5), 1083–1083. https://doi.org/10.1007/s00410-014-1083-6

MacQueen, J. (1967). Some methods for classification and analysis of multivariate observations. Paper presented at the Proceedings of the Fifth Berkeley Symposium on Mathematical Statistics and Probability, Volume 1: Statistics, Berkeley, Calif.

Mather, K. A., Pearson, D. G., McKenzie, D., Kjarsgaard, B. A., & Priestley, K. (2011). Constraints on the depth and thermal history of cratonic lithosphere from peridotite xenoliths, xenocrysts and seismology. *Lithos*, *125*(1–2), 729–742. https://doi.org/10.1016/j.lithos.2011.04.003

Maurya, S., Montagner, J. P., Ravi Kumar, M., Stutzmann, E., Kiselev, S., Burgos, G., et al. (2016). Imaging the lithospheric structure beneath the Indian continent. *Journal of Geophysical Research: Solid Earth*, *121*, 7450–7468. https://doi.org/10.1002/2016JB012948

McCammon, C. A. (2005). *Mantle oxidation state and oxygen fugacity: Constraints on mantle chemistry, structure, and dynamics* (pp. 219–240). Washington, DC: American Geophysical Union.

McCammon, C. A., Griffin, W. L., Shee, S. R., & O'Neill, H. S. C. (2001). Oxidation during metasomatism in ultramafic xenoliths from the Wesselton kimberlite, South Africa: Implications for the survival of diamond. *Contributions to Mineralogy and Petrology*, *141*(3), 287–296. https://doi.org/10.1007/s004100100244

McCammon, C. A., & Kopylova, M. G. (2004). A redox profile of the Slave mantle and oxygen fugacity control in the cratonic mantle. *Contributions to Mineralogy and Petrology*, *148*(1), 55–68. https://doi.org/10.1007/s00410-004-0583-1

McDonough, W. F., & Sun, S. S. (1995). The composition of the Earth. *Chemical Geology*, *120*(3–4), 223–253. https://doi.org/10.1016/0009-2541(94)00140-4

McLean, H., Banas, A., Creighton, S., Whiteford, S., Luth, R. W., & Stachel, T. (2007). Garnet xenocrysts from the Diavik mine, NWT, Canada: Composition, color, and paragenesis. *Canadian Mineralogist*, *45*(5), 1131–1145. https://doi.org/10.2113/gscanmin.45.5.1131

Mégnin, C., & Romanowicz, B. (1999). The effects of the theoretical formalism and data selection on mantle models derived from waveform tomography. *Geophysical Journal International*, *138*(2), 366–380. https://doi.org/10.1046/j.1365-246X.1999.00869.x

Meyer, H. O. A., Waldman, M. A., & Garwood, B. L. (1994). Mantle xenoliths from kimberlite near Kirkland Lake, Ontario. *The Canadian Mineralogist*, *32*, 295–306.

Michaut, C., Jaupart, C., & Bell, D. R. (2007). Transient geotherms in Archean continental lithosphere: New constraints on thickness and heat production of the subcontinental lithospheric mantle. *Journal of Geophysical Research*, *112*, B04408. https://doi.org/10.1029/2006JB004464

Michaut, C., Jaupart, C., & Mareschal, J.-C. (2009). Thermal evolution of cratonic roots. *Lithos*, *109*(1–2), 47–60. https://doi.org/10.1016/j.lithos.2008.05.008

Milman, V., Akhmatskaya, E. V., Nobes, R. H., Winkler, B., Pickard, C. J., & White, J. A. (2001). Systematic ab initio study of the compressibility of silicate garnets. *Acta Crystallographica Section B*, *57*(2), 163–177. https://doi.org/10.1107/S0108768100018188

Montagner, J. P., & Tanimoto, T. (1991). Global upper mantle tomography of seismic velocities and anisotropies. *Journal of Geophysical Research*, *96*(B12), 20,337–20,351. https://doi.org/10.1029/91JB01890

Morgan, P. (1984). The thermal structure and thermal evolution of the continental lithosphere. *Physics and Chemistry of the Earth*, *15*(Supplement C), 107–193. https://doi.org/10.1016/0079-1946(84)90006-5

Moulik, P., & Ekström, G. (2014). An anisotropic shear velocity model of the Earth's mantle using normal modes, body waves, surface waves and long-period waveforms. *Geophysical Journal International*, *199*(3), 1713–1738. https://doi.org/10.1093/gji/ggu356

Nataf, H.-C., Nakanishi, I., & Anderson, D. L. (1984). Anisotropy and shear velocities in the upper mantle. *Geophysical Research Letters*, *11*(2), 109–112. https://doi.org/10.1029/GL011i002p00109

Nehru, C. E., & Reddy, A. K. (1989). Ultramafic xenoliths from Vajrakarur kimberlites, India. *Geological Society of Australia Special Publications*, *14*, 745–758.

Nettles, M., & Dziewonski, A. M. (2008). Radially anisotropic shear velocity structure of the upper mantle globally and beneath North America. *Journal of Geophysical Research*, *113*, B02303. https://doi.org/10.1029/2006JB004819

Nita, B., Maurya, S., & Montagner, J.-P. (2016). Anisotropic tomography of the European lithospheric structure from surface wave studies. *Geochemistry, Geophysics, Geosystems*, *17*(6), 2015–2033. https://doi.org/10.1002/2015GC006243

Nixon, P. H. (1987). *Mantle xenoliths*. Chichester: Wiley.

Nixon, P. H., Rogers, N. W., Gibson, I. L., & Grey, A. (1981). Depleted and fertile mantle xenoliths from southern African kimberlites. *Annual Review of Earth and Planetary Sciences*, *9*(1), 285–309. https://doi.org/10.1146/annurev.ea.09.050181.001441

Nyblade, A. A., & Pollack, H. N. (1993). A global analysis of heat flow from Precambrian terrains: Implications for the thermal structure of Archean and Proterozoic lithosphere. *Journal of Geophysical Research*, *98*(B7), 12,207–12,218. https://doi.org/10.1029/93JB00521

Palyanov, Y. N., Bataleva, Y. V., Sokol, A. G., Borzdov, Y. M., Kupriyanov, I. N., Reutsky, V. N., & Sobolev, N. V. (2013). Mantle–slab interaction and redox mechanism of diamond formation. *Proceedings of the National Academy of Sciences of the United States of America*, *110*(51), 20,408–20,413. https://doi.org/10.1073/pnas.1313340110

Pearson, D. G. (1999). The age of continental roots. *Lithos*, *48*(1–4), 171–194. https://doi.org/10.1016/S0024-4937(99)00026-2

Pearson, D. G., Canil, D., & Shirey, S. B. (2003). Mantle samples included in volcanic rocks: Xenoliths and diamonds. In R. W. Carlson, H. D. Holland, & K. K. Turekian (Eds.), *The mantle and core*, *Treatise on Geochemistry* (Vol. 2, pp. 171–275). Amsterdam: Elsevier.

Pearson, D. G., Davies, G. R., Nixon, P. H., & Milledge, H. J. (1989). Graphitized diamonds from a peridotite massif in Morocco and implications for anomalous diamond occurrences. *Nature*, *338*(6210), 60–62. https://doi.org/10.1038/338060a0

Perry, H. K. C., Forte, A. M., & Eaton, D. W. S. (2003). Upper-mantle thermochemical structure below North America from seismic-geodynamic flow models. *Geophysical Journal International*, *154*(2), 279–299. https://doi.org/10.1046/j.1365-246X.2003.01961.x

Peslier, A. H., Woodland, A. B., Bell, D. R., & Lazarov, M. (2010). Olivine water contents in the continental lithosphere and the longevity of cratons. *Nature*, *467*(7311), 78–81. http://www.nature.com/nature/journal/v467/n7311/abs/nature09317.html#supplementary-information

Pollack, H. N. (1986). Cratonization and thermal evolution of the mantle. *Earth and Planetary Science Letters*, *80*(1–2), 175–182. https://doi.org/10.1016/0012-821X(86)90031-2

Pollack, H. N., & Chapman, D. S. (1977). On the regional variation of heat flow, geotherms, and lithospheric thickness. *Tectonophysics*, *38*(3–4), 279–296. https://doi.org/10.1016/0040-1951(77)90215-3

Poudjom Djomani, Y. H., O'Reilly, S. Y., Griffin, W. L., & Morgan, P. (2001). The density structure of subcontinental lithosphere through time. *Earth and Planetary Science Letters*, *184*(3–4), 605–621. https://doi.org/10.1016/S0012-821X(00)00362-9

Priestley, K., McKenzie, D., Debayle, E., & Pilidou, S. (2008). The African upper mantle and its relationship to tectonics and surface geology. *Geophysical Journal International*, *175*(3), 1108–1126. https://doi.org/10.1111/j.1365-246X.2008.03951.x

Pyle, J. M., & Haggerty, S. E. (1998). Eclogites and the Metasomatism of Eclogites from the Jagersfontein kimberlite: Punctuated transport and implications for alkali magmatism. *Geochimica et Cosmochimica Acta*, *62*(7), 1207–1231. https://doi.org/10.1016/S0016-7037(98)00040-4

Rader, E., Emry, E., Schmerr, N., Frost, D., Cheng, C., Menard, J., et al. (2015). Characterization and petrological constraints of the midlithospheric discontinuity. *Geochemistry, Geophysics, Geosystems*, *16*, 3484–3504. https://doi.org/10.1002/2015GC005943

Reichmann, H. J., Jacobsen, S. D., & Ballaran, T. B. (2013). Elasticity of franklinite and trends for transition-metal oxide spinels. *American Mineralogist*, *98*(4), 601–608. https://doi.org/10.2138/am.2013.4294

Rudnick, R. L., McDonough, W. F., & O'Connell, R. J. (1998). Thermal structure, thickness and composition of continental lithosphere. *Chemical Geology*, *145*(3–4), 395–411. https://doi.org/10.1016/S0009-2541(97)00151-4

Rudnick, R. L., McDonough, W. F., & Orpin, A. (1994). Northern Tanzanian peridotite xenoliths: A comparison with Kaapvaal peridotites and inferences on metasomatic interactions. In H. O. A. Meyer, & O. Leonardos (Eds.), *Proceedings of the 5th International Kimberlite Conference* (pp. 336–353). Brasilia: Companhia de Pesquisa de Recursos Minerais.

Schaeffer, A. J., & Lebedev, S. (2013). Global shear speed structure of the upper mantle and transition zone. *Geophysical Journal International*, *194*(1), 417–449. https://doi.org/10.1093/gji/ggt095

Schatz, J. F., & Simmons, G. (1972). Thermal conductivity of Earth materials at high temperatures. *Journal of Geophysical Research*, *77*(35), 6966–6983. https://doi.org/10.1029/JB077i035p06966

Schmickler, B., Jacob, D. E., & Foley, S. F. (2004). Eclogite xenoliths from the Kuruman kimberlites, South Africa: Geochemical fingerprinting of deep subduction and cumulate processes. *Lithos*, *75*(1–2), 173–207. https://doi.org/10.1016/j.lithos.2003.12.012

Schulze, D. J. (1989). Constraints on the abundance of eclogite in the upper mantle. *Journal of Geophysical Research*, *94*(B4), 4205–4212. https://doi.org/10.1029/JB094iB04p04205

Schulze, D. J., Wiese, D., & Steude, J. (1996). Abundance and distribution of diamonds in eclogite revealed by volume visualization of CT X-ray scans. *The Journal of Geology*, *104*(1), 109–114. https://doi.org/10.2307/30068066

Schutt, D. L., & Lesher, C. E. (2006). Effects of melt depletion on the density and seismic velocity of garnet and spinel lherzolite. *Journal of Geophysical Research*, *111*, B05401. https://doi.org/10.1029/2003JB002950

Sebai, A., Stutzmann, E., Montagner, J. P., Sicilia, D., & Beucler, E. (2006). Anisotropic structure of the African upper mantle from Rayleigh and Love wave tomography. *Physics of the Earth and Planetary Interiors*, *155*(1–2), 48–62. https://doi.org/10.1016/j.pepi.2005.09.009

Shapiro, S. S., Hager, B. H., & Jordan, T. H. (1999). The continental tectosphere and Earth's long-wavelength gravity field. *Lithos*, *48*(1–4), 135–152. https://doi.org/10.1016/S0024-4937(99)00027-4

Shervais, J. W., Taylor, L. A., Lugmair, G. W., Clayton, R. N., Mayeda, T. K., & Korotev, R. (1988). Archean oceanic crust and the evolution of sub-continental mantle: eclogites from Southern Africa. *Geological Society of America Bulletin*, *100*(3), 411–423. https://doi.org/10.1130/0016-7606(1988)100<0411:EPOCAT>2.3.CO;2

Shirey, S. B., Cartigny, P., Frost, D. J., Keshav, S., Nestola, F., Nimis, P., et al. (2013). Diamonds and the geology of mantle carbon. *Reviews in Mineralogy and Geochemistry*, *75*(1), 355–421. https://doi.org/10.2138/rmg.2013.75.12

Shirey, S. B., & Richardson, S. H. (2011). Start of the Wilson cycle at 3 Ga shown by diamonds from subcontinental mantle. *Science*, *333*(6041), 434–436. https://doi.org/10.1126/science.1206275

Smith, E. M., Shirey, S. B., Nestola, F., Bullock, E. S., Wang, J., & Richardson, S. H. (2016). Large gem diamonds from metallic liquid in Earth's deep mantle. *Science*, *354*(6318), 1403–1405. https://doi.org/10.1126/science.aal3303

Sobolev, N. V. (1977). *Deep-seated inclusions in kimberlites and the problem of the composition of the upper mantle*. Washington, DC: American Geophysical Union. https://doi.org/10.1029/SP011

Sokol, A. G., Pal'yanov, Y. N., Pal'yanova, G. A., Khokhryakov, A. F., & Borzdov, Y. M. (2001). Diamond and graphite crystallization from COH fluids under high pressure and high temperature conditions. *Diamond and Related Materials*, *10*(12), 2131–2136. https://doi.org/10.1016/S0925-9635(01)00491-5

Stachel, T., & Harris, J. W. (2008). The origin of cratonic diamonds—Constraints from mineral inclusions. *Ore Geology Reviews*, *34*(1-2), 5–32. https://doi.org/10.1016/j.oregeorev.2007.05.002

Stachel, T., & Luth, R. W. (2015). Diamond formation—Where, when and how? *Lithos*, *220-223*, 200–220. https://doi.org/10.1016/j.lithos.2015.01.028

Stagno, V., Ojwang, D. O., McCammon, C. A., & Frost, D. J. (2013). The oxidation state of the mantle and the extraction of carbon from Earth's interior. *Nature*, *493*(7430), 84–88. https://doi.org/10.1038/nature11679

Stixrude, L., & Lithgow-Bertelloni, C. (2005). Thermodynamics of mantle minerals—I. Physical properties. *Geophysical Journal International*, *162*, 610–632.

Stixrude, L., & Lithgow-Bertelloni, C. (2011). Thermodynamics of mantle minerals—II. Phase equilibria. *Geophysical Journal International*, *184*(3), 1180–1213. https://doi.org/10.1111/j.1365-246X.2010.04890.x

Tappert, R., Foden, J., Muehlenbachs, K., & Wills, K. (2011). Garnet peridotite xenoliths and xenocrysts from the Monk Hill kimberlite, South Australia: Insights into the lithospheric mantle beneath the Adelaide Fold Belt. *Journal of Petrology*, *52*(10), 1965–1986. https://doi.org/10.1093/petrology/egr036

Taylor, L. A., & Neal, C. R. (1989). Eclogites with oceanic crustal and mantle signatures from the Bellsbank kimberlite, South Africa. Part I: Mineralogy, petrography, and whole rock chemistry. *The Journal of Geology*, *97*(5), 551–567. https://doi.org/10.1086/629334

Thomassot, E., Cartigny, P., Harris, J. W., & Viljoen, K. S. (2007). Methane-related diamond crystallization in the Earth's mantle: Stable isotope evidences from a single diamond-bearing xenolith. *Earth and Planetary Science Letters*, *257*(3-4), 362–371. https://doi.org/10.1016/j.epsl.2007.02.020

Thybo, H., & Perchuć, E. (1997). The seismic 8° discontinuity and partial melting in continental mantle. *Science*, *275*(5306), 1626–1629. https://doi.org/10.1126/science.275.5306.1626

Valdez, M. N., Umemoto, K., & Wentzcovitch, R. M. (2012). Elasticity of diamond at high pressures and temperatures. doi: https://doi.org/10.1063/1.4754548

Vandersande, J. W., & Zoltan, L. D. (1991). High temperature electrical conductivity measurements of natural diamond and diamond films. *Surface and Coatings Technology*, *47*(1–3), 392–400. https://doi.org/10.1016/0257-8972(91)90305-G

Viljoen, K. S., Dobbe, R., Smit, B., Thomassot, E., & Cartigny, P. (2004). Petrology and geochemistry of a diamondiferous lherzolite from the Premier diamond mine, South Africa. *Lithos*, *77*(1–4), 539–552. https://doi.org/10.1016/j.lithos.2004.03.023

Viljoen, K. S., Swash, P. M., Otter, M. L., Schulze, D. J., & Lawless, P. J. (1992). Diamondiferous garnet harzburgites from the Finsch kimberlite, Northern Cape, South Africa. *Contributions to Mineralogy and Petrology*, *110*(1), 133–138. https://doi.org/10.1007/BF00310887

Walter, M. J., Kohn, S. C., Araujo, D., Bulanova, G. P., Smith, C. B., Gaillou, E., et al. (2011). Deep mantle cycling of oceanic crust: Evidence from diamonds and their mineral inclusions. *Science*, *334*(6052), 54–57. https://doi.org/10.1126/science.1209300

Weiss, Y., McNeill, J., Pearson, D. G., Nowell, G. M., & Ottley, C. J. (2015). Highly saline fluids from a subducting slab as the source for fluid-rich diamonds. *Nature*, *524*(7565), 339–342. https://doi.org/10.1038/nature14857

Whitmeyer, S. J., & Karlstrom, K. E. (2007). Tectonic model for the Proterozoic growth of North America. *Geosphere*, *3*(4), 220–259. https://doi.org/10.1130/GES00055.1

Woodland, A. B. (2009). Ferric iron contents of clinopyroxene from cratonic mantle and partitioning behaviour with garnet. *Lithos*, *112*(2), 1143–1149. https://doi.org/10.1016/j.lithos.2009.04.009

Woodland, A. B., & Koch, M. (2003). Variation in oxygen fugacity with depth in the upper mantle beneath the Kaapvaal craton, Southern Africa. *Earth and Planetary Science Letters*, *214*(1–2), 295–310. https://doi.org/10.1016/S0012-821X(03)00379-0

Workman, R. K., & Hart, S. R. (2005). Major and trace element composition of the depleted MORB mantle (DMM). *Earth and Planetary Science Letters*, *231*(1-2), 53–72. https://doi.org/10.1016/j.epsl.2004.12.005

Yaxley, G. M., Berry, A. J., Kamenetsky, V. S., Woodland, A. B., & Golovin, A. V. (2012). An oxygen fugacity profile through the Siberian Craton—Fe K-edge XANES determinations of Fe3+/SFe in garnets in peridotite xenoliths from the Udachnaya East kimberlite. *Lithos*, *140-141*, 142–151. https://doi.org/10.1016/j.lithos.2012.01.016

Yoshino, T., & Katsura, T. (2013). Electrical conductivity of mantle minerals: Role of water in conductivity anomalies. *Annual Review of Earth and Planetary Sciences*, *41*(1), 605–628. https://doi.org/10.1146/annurev-earth-050212-124022

Yoshizawa, K. (2014). Radially anisotropic 3-D shear wave structure of the Australian lithosphere and asthenosphere from multi-mode surface waves. *Physics of the Earth and Planetary Interiors*, *235*, 33–48. https://doi.org/10.1016/j.pepi.2014.07.008

Yuan, H., French, S., Cupillard, P., & Romanowicz, B. (2014). Lithospheric expression of geological units in central and eastern North America from full waveform tomography. *Earth and Planetary Science Letters*, *402*, 176–186. https://doi.org/10.1016/j.epsl.2013.11.057

Yuan, H., & Romanowicz, B. (2010). Lithospheric layering in the North American craton. *Nature*, *466*(7310), 1063–1068. https://doi.org/10.1038/nature09332

Zhang, B., & Yoshino, T. (2017). Effect of graphite on the electrical conductivity of the lithospheric mantle. *Geochemistry, Geophysics, Geosystems*, *18*, 23–40. https://doi.org/10.1002/2016GC006530

Zhang, Y. (1998). Mechanical and phase equilibria in inclusion-host systems. *Earth and Planetary Science Letters*, *157*(3-4), 209–222. https://doi.org/10.1016/S0012-821X(98)00036-3

Zhu, H., Bozdağ, E., Peter, D., & Tromp, J. (2012). Structure of the European upper mantle revealed by adjoint tomography. *Nature Geoscience*, *5*(7), 493–498. https://doi.org/10.1038/NGEO1501

Ziberna, L., & Klemme, S. (2016). Application of thermodynamic modelling to natural mantle xenoliths: Examples of density variations and pressure–temperature evolution of the lithospheric mantle. *Contributions to Mineralogy and Petrology*, *171*(2), 16. https://doi.org/10.1007/s00410-016-1229-9

Ziberna, L., Klemme, S., & Nimis, P. (2013). Garnet and spinel in fertile and depleted mantle: Insights from thermodynamic modelling. *Contributions to Mineralogy and Petrology*, *166*(2), 411–421. https://doi.org/10.1007/s00410-013-0882-5